A Moments View of Climatology and Variability of the Asian Summer Monsoon Anticyclone

Gloria L Manney*

NorthWest Research Associates & New Mexico Institute of Mining and Technology, Socorro, New Mexico, USA

Michelle L Santee

Jet Propulsion Laboratory, California Institute of Technology, Pasadena, California, USA.

Zachary D Lawrence†

Cooperative Institute for Research in Environmental Sciences (CIRES) & NOAA Physical Sciences Laboratory (PSL), University of Colorado, Boulder, Colorado, USA.

Krzysztof Wargan

Science Systems and Applications Inc., Lanham, MD, USA & NASA Goddard Space Flight Center, Greenbelt, Maryland, USA.

Michael J Schwartz

Jet Propulsion Laboratory, California Institute of Technology, Pasadena, California, USA.

**Corresponding author address:* Dept. of Physics, New Mexico Institute of Mining and Technology, Socorro, New Mexico, 87801, USA.

E-mail: manney@nwra.com

†Also at NorthWest Research Associates, Boulder, CO, USA.

ABSTRACT

A comprehensive investigation of the climatology of and interannual variability and trends in the Asian summer monsoon anticyclone (ASMA) is presented, based on a novel area and moments analysis. Moments include centroid location, aspect ratio, angle, and "excess kurtosis" (measuring how far the shape is from elliptical) for an equivalent ellipse with the same area as the ASMA. Key results are robust among the three modern reanalyses studied. The climatological ASMA is nearly elliptical, with its major axis aligned along its centroid latitude and a typical aspect ratio of $\sim$5–8. The ASMA centroid shifts northward with height, northward and westward during development, and in the opposite direction as it weakens. New evidence finding no obvious climatological bimodality in the ASMA reinforces similar suggestions from previous studies using modern reanalyses. Most trends in ASMA moments are not statistically significant. ASMA area and duration, however, increased significantly during 1979–2018; the 1958–2018 record analyzed for one reanalysis suggests that these trends may have accelerated in recent decades. ASMA centroid latitude is significantly positively (negatively) correlated with subtropical jet core latitude (altitude), and significantly negatively correlated with concurrent ENSO; these results are consistent with and extend previous work relating monsoon intensity, ENSO, and jet shifts. ASMA area is significantly positively correlated with the MEI ENSO index two months previously. These results improve our understanding of the ASMA using consistently defined diagnostics of its size, geometry, interannual variability, and trends that have not previously been analyzed.

1. Introduction

The Asian summer monsoon (ASM) anticyclone (ASMA; also known as the South Asian High or SAH) is a dominant feature of the boreal summer upper troposphere / lower stratosphere (UTLS) circulation, consisting of a vast upper-level anticyclonic vortex bounded by the subtropical westerly jet to the north and the tropical easterly jet (TEJ) to the south (e.g., Dunkerton 1995; Hsu et al. 1999; Zarrin et al. 2010). It is thought to arise primarily as a response to diabatic heating associated with land/sea contrasts and convection near the Tibetan and/or Iranian plateaus (Hoskins and Rodwell 1995; Qian et al. 2002; Liu et al. 2004, 2007; Garny and Randel 2013; Liu et al. 2013; Ren et al. 2019, and references therein). Strong intraseasonal and interannual variability in the ASMA is thought to be related to variations in topographic heating and/or dynamical influences originating from the subtropical jet or the tropics, but elucidating the details of these relationships is still an active area of study (Boos and Storelvmo 2016; Ge et al. 2018a; Ren et al. 2019; Xue and Chen 2019; Wu et al. 2020; Li et al. 2021, and references therein). Characterizing the ASMA and understanding its variability are critical because it is a primary factor affecting (and being affected by) major meteorological and transport processes in the boreal summer throughout the tropics and midlatitudes: for example, ASMA variations have been linked to shifts in tropical cyclone tracks (e.g., Kelly et al. 2018), and its feedbacks with rainfall variations have been widely studied (e.g., Bollasina et al. 2014; Wu et al. 2015; Nützel et al. 2016; Ge et al. 2018a,b; RavindraBabu et al. 2019; Wei et al. 2019; Xue and Chen 2019; Li et al. 2021). The ASMA also influences the composition of the entire summertime UTLS via convective lofting of near-surface air and subsequent quasi-horizontal transport (e.g., Garny and Randel 2016; Vogel et al. 2016; Pan et al. 2016; Santee et al. 2017; Nützel et al. 2019; Yan et al. 2019; Honomichl and Pan 2020, and references therein). While the ASMA has been extensively studied, because of the complexity of the system and the diversity of datasets and metrics used to study it, many questions remain – in characterizing the

ASMA, in elucidating the mechanisms driving its variability, and in understanding its role in the ASM system and links to UTLS composition.

The ASMA has been defined in numerous ways (see, e.g., Santee et al. 2017; Yan et al. 2019, for brief summaries), and that definition influences the information and insights gained from ASMA studies. ASMA position, extent, and intensity are most commonly defined using fields, gradients of, or anomalies in 100 to 200 hPa geopotential height (GPH) (Zarrin et al. 2010; Nützel et al. 2016; Pan et al. 2016; Barret et al. 2016, and references therein) or in UTLS PV (Garny and Randel 2013; Ploeger et al. 2015; Amemiya and Sato 2018, and references therein). Some studies have also used streamfunction (e.g., Tweedy et al. 2018; Yan et al. 2018) or Montgomery Streamfunction (MSF) on isentropic surfaces (e.g., Popovic and Plumb 2001; Fairlie et al. 2014; Santee et al. 2017). Studies that track ASMA latitude typically identify its "ridgeline" using relative vorticity, GPH, or wind changes (e.g., Zhang et al. 2002; Zarrin et al. 2010; Nützel et al. 2016). Most often, these metrics are defined on a single level. PV-based metrics are especially difficult to define because PV provides a closed contour in the ASMA region only in a very narrow potential temperature range (e.g., Garny and Randel 2013; Ploeger et al. 2015; Santee et al. 2017). One motivation for using PV-based metrics is the analogy of the ASMA to the stratospheric polar vortex as a transport barrier; Garny and Randel (2013) and Ploeger et al. (2015) both noted that the ASMA can be viewed similarly to that closed circulation in many respects but represents a much "leakier" transport barrier, especially on its equatorward side.

We exploit the polar vortex analogy in a different way in this work: Motivated by the efficacy of the method for characterizing the size, geometry, vertical structure, preferred locations, and evolution of the stratospheric polar vortex (e.g., Waugh and Randel 1999; Matthewman et al. 2009; Lawrence and Manney 2018), we apply a moments and area analysis to the ASMA defined using MSF as in Santee et al. (2017). One advantage of using MSF is that a closed circulation can be defined over a much wider range of isentropic levels than for PV-based diagnostics (e.g., Ploeger et al. 2015; Santee et al. 2017); Santee et al. (2017) also showed that the MSF-based definition they used closely reflected the ASMA transport barrier as seen in trace gas observations. Using the moments and area diagnostics, we conduct a comprehensive analysis of variability and trends in the ASMA's size, geometry, and position. Our synthesis of ASMA variability and trends based on these unique consistently defined metrics provides new insight into outstanding questions about the ASMA (discussed further below), including the existence and/or character of ASMA "bimodality" and the relationships of ASMA variability to El Niño / Southern Oscillation (ENSO), the Quasi-biennial Oscillation (QBO), and the subtropical upper tropospheric (UT) jet.

We focus on three recent reanalyses that have been shown to provide robust results for UTLS studies. Reanalysis datasets are one of the most powerful tools available to characterize large-scale dynamical processes, but they must be used with care since the underlying forecast models and data assimilation systems they rely on have limitations (e.g., Fujiwara et al. 2017). Numerous studies highlight the importance of comparing results from multiple reanalyses for UTLS studies (e.g., Manney et al. 2017; Manney and Hegglin 2018; Xian and Homeyer 2019; Tegtmeier et al. 2020; Wright et al. 2020), including a few focusing on aspects of the ASMA (e.g., Wu et al. 2017; Shi et al. 2018). In a detailed reanalysis comparison, Nützel et al. (2016) showed the archaic National Center for Environmental Prediction/National Center for Atmospheric Research (NCEP-R1) and NCEP/Department of Energy (NCEP-R2) reanalyses to be outliers that are inappropriate for detailed study of the ASMA. Older reanalyses such as these have long been deprecated for stratospheric and UTLS studies (e.g., Pawson and Fiorino 1998; Randel et al. 2000; Manney et al. 2003, 2005b,a; Fujiwara et al. 2017; Homeyer et al. 2021; Tegtmeier et al. 2021, and references therein). Nevertheless, a multitude of previous studies on ASMA climatology and variability have relied on NCEP-R1 and/or NCEP-R2, including many published since Nützel et al. (2016) showed these products to be unsuitable for ASMA studies (e.g., Preethi et al. 2017; Wang et al. 2017; Xue et al.

2017; Feba et al. 2019; Xue and Chen 2019; Ren et al. 2019; Samanta et al. 2020; Seetha et al. 2020; Yang et al. 2020; Basha et al. 2020; Wu et al. 2020).

One open question for which the choice of reanalysis product is critical is the existence or character of ASMA bimodality, that is, preferred locations over the Tibetan and Iranian Plateaus (e.g., Qian et al. 2002; Zhang et al. 2002; Zhou et al. 2009; Zarrin et al. 2010; Yan et al. 2011; Pan et al. 2016). Nützel et al. (2016) found strong evidence for bimodality only in NCEP-R1 and limited evidence in NCEP-R2; they found no evidence for it in more modern reanalyses for daily, pentad, or seasonal data, and only limited evidence in monthly data. Other studies using more recent reanalyses have not seen evidence for bimodality (e.g., Garny and Randel 2013; Ploeger et al. 2015).

Many studies of ASM variability and trends have focused on near-surface fields such as rainfall and low-level temperatures or winds (e.g., Kajikawa et al. 2012; Preethi et al. 2017; Kodera et al. 2019; Brönnimann et al. 2016; Wu et al. 2020, and references therein), and some suggest a trend towards earlier monsoon onset in spring, with possible relationships to anthropogenic forcing (e.g., Kajikawa et al. 2012; Bollasina et al. 2013, 2014; Bombardi et al. 2020). Near-surface metrics have been linked to the upper-level circulation, with, for example, westward and northward trends in the UT anticyclonic circulation associated with corresponding interannual variability in surface conditions (e.g., Preethi et al. 2017); links between interannual variability in ASM precipitation onset and tropopause variations (e.g., RavindraBabu et al. 2019); and evidence of UT subtropical jet changes (weakening or latitude changes) associated with earlier monsoon onset (e.g., Samanta et al. 2020; Wu et al. 2020). The UT subtropical jet shifts northward around the ASMA in summer (e.g., Manney et al. 2014), so variability in the ASMA is expected to be closely linked to that of the UT jets, as suggested by previous studies (Schiemann et al. 2009; Manney et al. 2014; Manney and Hegglin 2018; Wu et al. 2020; Chen et al. 2021; Li et al. 2021; Zhu et al. 2021, and references therein), but the relationships have not been comprehensively studied.

Studies of the relationship of the ASM system to natural modes of variability such as ENSO the QBO have also not resulted in a consensus. Numerous studies have explored the relationships between the ASM and sea surface temperature (SST) variability such as ENSO (e.g., Ju and Slingo 1995; Wang et al. 2001; Li et al. 2017; Liu et al. 2017; Tweedy et al. 2018; Yan et al. 2018; Basha et al. 2020, and references therein) using a variety of local and regional metrics to define monsoon onset and intensity (see, e.g., Bombardi et al. 2020, for a review). Several studies have observed or simulated an association of preceding El Niño conditions with later monsoon onset and/or weaker monsoon activity (e.g., Ju and Slingo 1995; Webster et al. 1998; Wang et al. 2013; Basha et al. 2020, and references therein), including studies using ASM intensity or position indices related to the UT circulation (e.g., Tweedy et al. 2018; Yan et al. 2018). However, counter-examples and dependence on ENSO type and timing relative to monsoon onset are also reported (e.g., Yuan and Yang 2012; Wang et al. 2013; Li et al. 2017; Liu et al. 2017; Hu et al. 2020). Moreover, recent work suggests changes in the relationship between ENSO and the ASM since the 1990s, which may be associated with UT jet changes (e.g., Feba et al. 2019; Hrudya et al. 2020; Samanta et al. 2020; Seetha et al. 2020, and references therein). For the QBO, some studies have suggested a positive correlation between QBO and ASM intensity (e.g., Mukherjee et al. 1985; Giorgetta et al. 1999), while others have not found consistent correlations (e.g. Claud and Terray 2007; Brönnimann et al. 2016).

The new diagnostics described above, derived from robust modern reanalysis datasets, allow us to tackle these outstanding questions in a unified framework. Our work is organized as follows: Section 2 describes the reanalysis datasets and methods used. Section 3a shows a detailed moments and area climatology; Section 3b1 reports a trend analysis; Section 3b2 shows correlations with ENSO, QBO, and the subtropical jet; and Section 3c investigates the longer-term record from the most recent reanalysis dataset from the Japan Meteorological Agency (JMA). Conclusions are presented in Section 4.

2. Data and Methods

a. Reanalysis Datasets

We present the moments and area analysis (see Section 2b below) based on three recent "full-input" reanalyses (that is, those that assimilate a full suite of satellite and conventional measurements, see, e.g., Fujiwara et al. 2017): the GMAO MERRA version-2 (MERRA-2) reanalysis (Gelaro et al. 2017); the ECMWF ERA-Interim reanalysis (Dee et al. 2011); and the JMA 55-year reanalysis (JRA-55) (Ebita et al. 2011; Kobayashi et al. 2015). Models, assimilation systems, and data inputs for these reanalyses are described by Fujiwara et al. (2017). We analyze the climatology and variability of the ASMA moments and area for 1979 through 2018. Calculations are done using daily 12-UT fields from each reanalysis dataset, whose fields are used on their native model levels and at or (in the case of spectral models) near their native horizontal resolution. We use the JRA-55C "conventional input" (that is, no satellite data, see Kobayashi et al. 2014) reanalysis for 1973–2012 to evaluate how JRA-55 might differ in the pre-satellite (before 1979) and satellite periods. This informs our analysis of the full JRA-55 record from 1958–2018.

1) MERRA-2

MERRA-2 (Gelaro et al. 2017) uses 3D-Var assimilation with Incremental Analysis Update (IAU) (Bloom et al. 1996) to constrain the analyses. MERRA-2 data products on model levels and a $0.5^\circ \times 0.625^\circ$ latitude/longitude grid are used. MERRA-2 has 0.8 km vertical spacing in the UT, increasing to $\sim$1.2 km in the lower stratosphere. Data from the MERRA-2 spin-up year, 1979, are included here. The MERRA-2 "Assimilated" data collection (Global Modeling and Assimilation Office (GMAO) 2015) used here is recommended by GMAO for most studies.

2) ERA-Interim

ERA-Interim (see Dee et al. 2011) is a global reanalysis covering 1979 through August 2019. The data are produced using 4D-Var assimilation. ERA-Interim data are used on a $0.75^\circ \times 0.75^\circ$ latitude/longitude grid, and have about 1-km spacing in the UTLS.

3) JRA-55

JRA-55 (Ebita et al. 2011; Kobayashi et al. 2015) is a global reanalysis covering 1958 to the present. The data are produced using a 4D-Var assimilation. They are provided on an approximately 0.56° Gaussian grid corresponding to that spectral resolution. The vertical spacing of the JRA-55 fields on model levels is nearly identical to that of ERA-Interim in the UTLS (e.g., see Fig. 3 in Fujiwara et al. 2017). The JRA-55C reanalysis (covering November 1972 through 2012, see, e.g., Kobayashi et al. 2014) uses the same model and grids but does not assimilate satellite data.

b. Methods

1) ASMA Diagnostics

Following Santee et al. (2017), we use contours of daily 1200UT MSF on the 350 K (MSF value 344800 $\mathrm{m^2 s^{-2}}$), 370 K (356500 $\mathrm{m^2 s^{-2}}$), 390 K (367100 $\mathrm{m^2 s^{-2}}$), and 410 K (377300 $\mathrm{m^2 s^{-2}}$) isentropic surfaces to define the ASMA boundary, covering pressure (altitude) ranges from approximately 250 hPa (10 km) to 70 hPa (19 km). Santee et al. (2017) determined the listed values by analyzing MSF correlations with windspeed, thus approximating the MSF values at the locations of strong windspeed gradients demarking the transport barriers associated with the bounding jets. The those jets agree well in the reanalyses used herein (Manney et al. 2017), so we expect that these values provide a reasonable approximation to that transport barrier for each of the reanalyses. Using a single value provides a consistent metric for assessing reanalysis differences, which may legitimately include small biases in MSF values. Sensitivity tests for several case studies show that our results are insensitive to small changes in the MSF value used.

The ASMA is identified in the region between 0 and 175° longitude and 0 and 60° latitude (hereinafter the "ASM box"). This box is larger than that used in Santee et al. (2017) and most previous studies (e.g., Bergman et al. 2013; Ploeger et al. 2015; Garny and Randel 2016; Zhang et al. 2016) to ensure that it usually encompasses the entire ASMA throughout the monsoon season. Inspection of the regions defined as inside the ASMA using this larger box showed no evidence of areas not associated with the ASMA; even this larger box occasionally cuts off a small portion of the ASMA region, but such cases are uncommon.

The ASMA is characterized using a moments analysis similar to that used to describe stratospheric polar vortex characteristics (Waugh and Randel 1999; Matthewman et al. 2009; Mitchell et al. 2011; Lawrence and Manney 2018, and references therein). The calculations are based on the algorithms of Lawrence and Manney (2018) (which in turn followed those of Matthewman et al. 2009), except that the Cartesian grid used is a cylindrical equal area grid covering the ASM box mentioned above, and MSF fields are used instead of PV. As described in detail by Matthewman et al. (2009), this analysis computes moments of the equivalent ellipse and then uses them to calculate the centroid latitude and longitude, aspect ratio (calculated in the cylindrical equal-area projection), angle (measured counterclockwise from the centroid latitude), and excess kurtosis (EK); hereinafter we use the term "moments" to describe those derived quantities. EK has been used as a method of identifying polar vortex splits (e.g., Matthewman et al. 2009; Matthewman and Esler 2011).

ASMA area is calculated as the fraction of the total hemispheric area within the ASM box with MSF greater than the threshold value. For each day, area values less than 1% of a hemisphere are filtered out to limit large day-to-day variability in identification of ASMA existence at the beginning and end of the season because of the presence of very small transient regions with

MSF greater than the edge values (similar to the filtering commonly used in stratospheric polar vortex identification, Manney and Lawrence 2016; Lawrence and Manney 2018, and references therein). Figures S1 and S2 in the supplementary information (hereinafter SI) show example maps illustrating the ASMA edge, equivalent ellipse, and centroid locations.

Gridpoints at the ASMA edge are identified using the Canny edge detection algorithm (Canny 1986). For analysis of ASMA start and end dates and duration, the season is considered to begin (end) when the area with MSF exceeding the boundary value has been greater than 1% of a hemisphere (the general area threshold mentioned above) for 20 consecutive days before (after) the start (end) date. We tested the sensitivity to several area (from 0.5% to 2% of a hemisphere) and persistence (from 10 to 30 days) thresholds; the values chosen ensure that the results are not noticeably biased (particularly in comparisons between different reanalyses) by small transient regions above the thresholds.

2) ANALYSIS

The diagnostics described above are used to calculate climatological monthly (April through October) and seasonal (June–July–August, JJA) means and frequency distributions of the ASMA edge and centroid locations. We construct climatological time series of the moments and area, as well as diagnosing trends in moments, area, and duration diagnostics over the 40-year period. We show correlations of these timeseries with ENSO, QBO, and subtropical UT jet stream variations.

Trends are analyzed as in Manney and Hegglin (2018) using a linear regression of the monthly and seasonal mean time series of moments and area diagnostics, and assessing the statistical significance using a permutation analysis (e.g., Wilks 2011, Section 5.3.4) wherein the 40-year time series for each time period (month, season) are randomly shuffled to produce 100,000 possible arrangements of the values. A two-sided p-value is derived by counting how many permuted slopes have larger magnitude than those derived from the reanalyses and dividing by the number of instances (100,000) in the permutation distributions. Consistency among the reanalyses is also critical in assessing the robustness of trends (e.g., Manney and Hegglin 2018). Relationships with ENSO are assessed using correlations with the Multivariate ENSO Index (MEI, Wolter and Timlin 2011). (Correlations of ASMA characteristics with the MEIv2 give very similar results, as do, with slightly larger differences as expected from using an index defined using SSTs averaged in different regions, correlations with the Niño3.4 index; these differences do not qualitatively change any of our results). Relationships with the QBO are examined using correlations with 50 and 70 hPa Singapore winds (from the Freie Universität Berlin, Naujokat 1986) and with 30–50 hPa wind shear. The correlations are also done with ± 2 and ± 1 month lags. All of the timeseries used are detrended prior to calculating correlations.

We also examine correlations with the subtropical UT jet streams' latitude, altitude, and windspeed from JETPAC (JEt and Tropopause Products for Analysis and Characterization, Manney et al. 2011a, 2014, 2017; Manney and Hegglin 2018); the subtropical jet is identified (as described by Manney and Hegglin 2018) in a physically meaningful way as the jet across which the "tropopause break" occurs. We examined zonally averaged jet characteristics, as well as jet characteristics averaged over longitude bands; the strongest correlations are in the 45–90°E and 80–160°E longitude bands (as expected since those bands are within the typical region of the ASMA), and we illustrate the results showing the latter here.

To assess the statistical significance of correlations, we use bootstrap resampling (e.g., Elfron and Tibshirani 1993), resampling the time series 100,000 times. We use this to construct 95 and 99% confidence intervals for the correlations. (See Lawrence et al. 2018; Lawrence and Manney 2020, for further details of the bootstrapping methods).

3. Results

a. Climatology of ASMA Moments and Area

Figure 1 shows the climatological mean ASMA edge and centroid locations at 350 and 390 K for each reanalysis during individual months, and frequency distributions at the same levels of the centroid and edge locations in JJA. (Fig. S3 shows mean edge and centroid locations for all levels as well as for JJA.) Centroid locations typically agree well among the reanalyses, especially when the ASMA is fully developed in July and August. The ASMA is larger in MERRA-2 than in the other reanalyses; ERA-Interim typically has the smallest area, but it is closer to that of JRA-55 than JRA-55 is to MERRA-2. The largest differences, at 350 K, arise primarily from a more equatorward southern edge and larger longitudinal extent of the ASMA in MERRA-2. The appearance of only centroid locations (for most reanalyses at most levels in May and September) indicates that mean values were above the edge threshold at only one or two gridpoints. Only MERRA-2 at 350 K shows a significant region of values exceeding the threshold in May. In June, the ASMA is larger at 370 K and 390 K than at 350 K and 410 K (Fig. S3, also consistent with Santee et al. 2017), except in MERRA-2, which shows a much larger area than the other reanalyses at 350 K. Consistent with previous findings based on other ASMA diagnostics (e.g., Randel and Park 2006; Bergman et al. 2013; Ploeger et al. 2015; Santee et al. 2017, and references therein), the centroid location shifts north (and sometimes slightly east) with height. The location of the centroids well east of the center of the ASMA region in September at 350 K (and 370 K, Fig. S3) arises primarily from the common occurrence of a small local maximum to the east, either split off from or attached by a narrow tongue to the main ASMA (e.g., as in eddy-shedding events, Popovic and Plumb 2001; Honomichl and Pan 2020), which affects the centroid location more than it does the mean edge.

Except at 350 K, the distributions for the three reanalyses agree well, but with the larger MERRA-2 area reflected in the edge distributions. Broader and less sharply peaked frequency distributions at 350 K than at higher levels (e.g., 390 K shown here) indicate larger variability at that level. The MERRA-2 350-K centroid distribution is "tilted" east and south with respect to those for ERA-Interim and JRA-55, and its more diffuse edge distribution indicates greater variability. All of the reanalyses show a fairly uniform maximum along the southern edge from about 30°E to 120°E. In contrast, there is a localized maximum at the northern edge just west of 90°E (though not as consistently, especially for MERRA-2, at 350 K), indicating a preferred position along that edge. This position ($\sim$40°N, $\sim$85°E, near the northern edge of the Tibetan Plateau) coincides with the preferred location of the subtropical westerly jet in JJA (Manney et al. 2014) and is consistent with the approximate position of the northern edge towards the eastern side in three of the four "phases" of the ASMA described by Pan et al. (2016).

The fields in Fig. 1 do not show evidence of bimodality. This supports the analysis of Nützel et al. (2016) showing strong bimodality in NCEP-R1 and NCEP-R2 (which are deprecated for UTLS studies, Homeyer et al. 2021; Tegtmeier et al. 2021, and references therein) but not in modern reanalyses including MERRA, ERA-Interim, and JRA-55. Our results are also consistent with the moments analysis for MERRA and NCEP Climate Forecast System Reanalysis / version 2 (CFSR/CFSv2) (S-RIP Chapter 8, Tegtmeier et al. 2021), and with the lack of a clear bimodality signature in other studies using recent reanalyses (e.g., Garny and Randel 2013; Ploeger et al. 2015). Our climatological results do not preclude the occurrence of bimodal geometries (such as the "Tibetan Plateau", "Iranian Plateau", or "Double-center" phases shown by Pan et al. 2016) over short periods or on individual days; indeed, such geometries are seen in some of the example maps in Fig. S2.

Figure 2 shows the climatological seasonal evolution of the ASMA. The moments climatologies agree well among the reanalyses at 370, 390, and 410 K once the circulation is well developed. This is also apparent in JJA histograms (centroid latitude, centroid longitude, and area in Fig. 3; aspect ratio and angle in Fig. S4). At 350 K, MERRA-2 has the highest (farthest east) centroid longitudes until August and ERA-Interim the lowest. MERRA-2 350-K centroid latitudes are slightly lower throughout the season, with the largest differences (about 5°) early and late in the season and about 3° differences in JJA (Figure 3).

The ASMA centroid location shifts northward and westward during ASMA development, and southward and eastward after the peak of the ASMA season (Fig. 2). Strongest shifts are at 350 K, where the climatological position is near 15°N, 120°E in May; near 30°N, 75°E by August; and near 25°N, 125°E by October. These values are consistent with the 10–15° latitude / ∼30° longitude shifts at 100 hPa noted by Nützel et al. (2016). This behavior is in line with other previous studies, some suggesting that it arises from seasonal heating changes on the Iranian and Tibetan Plateaus, which may also affect ASM rainfall and thus feed back on ASMA development, location, and duration (e.g., Qian et al. 2002; Wu et al. 2015, 2020). Mean centroid latitudes in JJA (and their maxima) are about 25–28 (29–31), 29–30 (32), 32 (34), and 35 (37) degrees north at 350, 370, 390, and 410 K, respectively, with the ranges reflecting reanalysis differences (Figs. 2 and 3). The JJA-mean centroid longitude is near 80°E at all levels. Although the period over which the ASMA is consistently well defined is shorter at higher levels (also seen in Fig. S3), the area increases faster at 370 and 390 K than at 350 K, so, except in MERRA-2, the areas at these higher levels are larger than that at 350 K by June. The UT subtropical jet core is climatologically near 350 K (e.g., Manney et al. 2014), with winds weakening and shifting northward with height; the northward shift of geopotential height gradients associated with that is consistent with a northward shift of the ASMA with height.

The aspect ratio of the ASMA equivalent ellipse typically ranges between 5 and 10 when the circulation is well defined (Fig. 2), with a JJA mean of around 8 at 350 K and 7 at the higher levels (Fig. S4). At 350 K, the aspect ratio increases from about 3 to 8–9 during June and then remains nearly flat until gradually decreasing again starting in mid-September. At the higher levels, the aspect ratio increases gradually from 3–5 to 7–9 through the season (until late-September, mid-

September, and mid-August at 370, 390, and 410 K, respectively). Larger peaks (exceeding 20) for individual dates/years tend to cluster near the end of the season, when splitting or pinching off of sub-vortices often results in an elongated ASMA.

The ASMA angle typically ranges between about $\pm 5°$ when the ASMA is well defined, with a tendency towards slightly negative values before mid-season (Fig. 2) and a JJA-mean very near zero (Fig. S4). Larger negative values (up to about $-10°$) at 350 K through June indicate that the eastern side of the ASMA often tilts equatorward during this period.

EK is a combination of higher-order moments defined such that negative values indicate a "pinched" shape, zero indicates an elliptical vortex, and positive values indicate a "diamond-shaped" vortex or one with extensive filamentation (Matthewman et al. 2009). Negative values have been used to indicate stratospheric polar vortex splitting, e.g., -0.1 by Matthewman et al. (2009) and -0.6 by Matthewman and Esler (2011). Except at 350 K, ASMA EK is typically slightly positive; significantly negative values are uncommon in this climatology (Fig. S5). Statistics of negative EK by year and month (Fig. S6) show only a few instances at 370, 390, or 410 K with extended periods of negative EK (e.g., July and August 1989 at 370 and 390 K). Daily MSF maps at these times (e.g., Fig. S2) indicate that negative EK is associated with a pinched ASMA shape (similar to the "western (Iranian plateau)" or "double-center" phases described in Pan et al. 2016); one of the MSF maxima in these cases is typically near the Iranian Plateau (around 40–60°E longitude), consistent with one of the preferred locations in studies suggesting bimodality (Nützel et al. 2016, and references therein), while the location of the other varies considerably. ASMA splitting occurs for negative EK magnitudes as small as about 0.25; on the other hand, the ASMA may remain unsplit for negative EK magnitudes as large as 0.65 (the latter cases are either nearly split or associated with elongated sinuous ASMA shapes). Thus, periods of negative EK do signify particular ASMA structures, but they are uncommon and are not a specific indicator of splitting. Large positive EK values are fairly common (and would occur in situations similar to the "eastern (Tibetan Plateau)" phase of Pan et al. 2016), but their small effect on climatological EK suggests that they occur only for short periods in individual years (most frequently early and late in the ASM season). Slightly positive mean EK values suggest that the ASMA is most often close to elliptical or has a slight bulge along the minor axis. Further exploration of the details of ASMA structure leading to large variations in EK may be useful for case studies, but the complexity of correlating this diagnostic with consistent morphologies is beyond the scope of this paper.

At 370, 390, and 410 K, MERRA-2 areas are 15–20% larger than those in the other reanalyses (Figs. 2 and 3). At 390 and 410 K, ERA-Interim areas are 5–10% smaller than those in JRA-55. At 350 K, MERRA-2 areas are 40–50% larger than those for the other reanalyses, consistent with the edge locations shown in Fig. 1. The MERRA-2 range includes more high values at all times, and thus peaks in the mean are less distinct (clearly apparent in JJA in Fig. 3 and reflected in more diffuse edge distributions in Fig. 1).

The area in Fig. 2 indicates that the ASMA starts developing in late April at 350 K and in early May to early June at higher levels. At each level, a peak in mid-May (strongest at 350 and 370 K) is followed by a rapid but brief decrease and then a steady rise until late July/early August. The late-May area peak arises almost entirely from three years: 1998, 2010, and 2016. Although the area drops abruptly near the end of May in those years (producing an apparent climatological minimum in early June), these years remain among those with the largest area through the peak of the monsoon season (see Section 3b). ASMA area increases more slowly at 350 K than at higher levels. In MERRA-2, the maximum climatological ASMA area is about 12% of a hemisphere at 350 K and about 10% at the higher levels; the other reanalyses show a maximum climatological area of about 7% at 350 K, and slightly under 10% at the higher levels. For comparison, this maximum area is similar to that of the Arctic stratospheric polar vortex in a typical winter (see, e.g., Manney et al. 2011b; Garny and Randel 2013; Manney and Lawrence 2016). Previous studies have shown qualitatively similar seasonal evolution of area-related diagnostics such as grid-point counts or east/west extent (e.g., Qian et al. 2002; Liu et al. 2017; Xue et al. 2017; Xue and Chen 2019).

b. Variability and Trends

1) Interannual Variability and Trends in the ASMA

Considerable interannual variability is seen in the ASMA moments and area (Fig. 4 shows area in JJA; Fig. S7 shows other moments). This variability is qualitatively very consistent in all of the reanalyses, but the differences seen in the climatology are reflected in relative biases between the values, especially at 350 K. Although trends from reanalyses must be treated with caution (because of step-changes in data inputs and differences in how each reanalysis handles such changes, e.g., Oliver 2016; Fujiwara et al. 2017; Long et al. 2017; Manney and Hegglin 2018; Bao and Zhang 2019, and references therein), ASMA area shows strong evidence for increasing trends that are consistent among the reanalyses.

Figure 5 summarizes the linear trends in the area time series shown in Fig. 4. Trends are positive in all reanalyses, in all months and during JJA, and at all levels except 410 K in September. Most of these trends are significant at the 95% confidence level except in September, when only 350 K shows consistently significant trends. JRA-55 trends are also insignificant in August at 390 and 410 K and in June and JJA at 410 K, and ERA-Interim and JRA-55 trends are insignificant in June at 390 K. MERRA-2 area trends are larger than those in the other reanalyses at all levels. We have previously done this trend analysis for periods ending in 2014, 2015, and 2017, with very similar results (see S-RIP chapter 8, Tegtmeier et al. 2021, for a 370 K example through 2015), indicating that within the 2014–2018 interval the results are not strongly affected by outliers in the end dates (consistent with the general absence of extreme values at the end points of the time series shown in Fig. 4). These results suggest a robust increasing trend in ASMA area over the past approximately 40 years.

Figure 6 shows start and end dates and duration (end minus start date) of the ASMA (see Section 2b for details). The interannual variability agrees qualitatively among the reanalyses, but MERRA-2 shows substantially longer ASM seasons at 350 K than the other reanalyses, consistent with its larger area at that level. Mean formation dates are earlier at lower levels in JRA-55 and MERRA-2 (e.g., mean values for JRA-55 – typically the "middle" of the three reanalyses – are 30 May, 30 May, 6 June, and 16 June at 350, 370, 390, and 410 K, respectively). The earliest mean start date for ERA-Interim is 4 June at 370 K.

End dates in MERRA-2 and JRA-55 are later at lower levels (e.g., JRA-55 mean of 17 September, 15 September, 10 September, and 3 September at 350, 370, 390, and 410 K, respectively), while the latest ERA-Interim end date is 12 September at 370 K. Together, these results lead to the longest mean duration at 350 K for MERRA-2 and JRA-55 (159 and 110 days, respectively) and at 370 K for ERA-Interim (100 days). These results are consistent with and help quantify the reanalysis differences in ASMA area shown above.

The linear fits in Fig. 6 show trends towards earlier formation dates, later decay dates, and longer lifetimes at all levels, consistent with the area trends discussed above. These trends are much larger at 350 K (37, 53, and 41 days longer in 2018 than in 1979 for MERRA-2, ERA-Interim, and JRA-55, respectively) than at higher levels (ranging from 7 to 24 days 2018−1979 difference, depending on level and reanalysis). Figure 7 summarizes these trends and their significance. Consistent with the area increase, these trends are larger at 350 K than at higher levels and larger in MERRA-2 than in other reanalyses. 410 K trends are not significant except for MERRA-2 decay dates and lifetime; 390 K trends in all quantities in JRA-55 and in decay date in ERA-Interim are also not significant.

Figures S7 and S8 show that, despite consistent slopes among the reanalyses in many cases, few of the apparent trends in other diagnostics are significant at the 95% confidence level. Positive trends in aspect ratio in July at 390 and 410 K, and in JJA at 370 and 390 K, are significant and consistent among the reanalyses. Significant positive trends are also seen in angle at 370, 390, and 410 K in July, although the angle remains quite small.

2) ASMA Correlations with Upper Tropospheric Jets, ENSO, and QBO

Figure 8 show correlations of ASMA centroid latitude and area with the subtropical UT jet core latitude and altitude at 350 and 390 K in the 80–160° longitude region (Figs. S9 and S10 show correlations of jet locations with other moments and at the other levels). Similarly strong correlations are seen in the 45–90° longitude region, and weaker ones of consistent sign are seen in the zonal mean (not shown). ASMA centroid latitude is the moment that shows the strongest correlation with subtropical jet location, with mostly significant positive (negative) correlations with subtropical jet latitude (altitude). Weaker/less significant correlations are seen in September; similar (though usually less significant) correlations are seen at the other levels (Figs. S9 and S10). Since the core of the subtropical jet sits near 350 K (e.g., Manney et al. 2014; Santee et al. 2017), weaker correlations at higher levels are expected. The positive correlation of ASMA centroid latitude with jet latitude is consistent with the northward shift of the subtropical jet around the poleward edge of the ASMA (typically to a maximum latitude near 42–45°N) during boreal summer (e.g., Schiemann et al. 2009; Manney et al. 2014; Manney and Hegglin 2018). This poleward subtropical jet shift has been linked to monsoon-related heating; such heating, which is stronger for more intense monsoons, increases the temperature gradients north of the jet, inducing a northward jet shift via the thermal wind relationship (e.g., Schiemann et al. 2009; Ge et al. 2018a,b). Since the climatological equatorward ASMA edge location does not vary much (see, e.g., more sharply peaked equatorward edge distributions in Fig. 1 and sharply peaked TEJ distributions in Manney et al. 2014), its poleward edge is expected to expand more, increasing centroid latitude, with increasing area. A positive centroid latitude / subtropical jet latitude correlation is thus expected if ASMA area is positively correlated with monsoon intensity (a reasonable supposition, though details of area / intensity relationships would likely be complex and depend on the metric). ASMA area is usually negatively (positively) correlated with subtropical jet latitude (altitude), but only correlations with altitude show significant values for all reanalyses at 350 and 370 K in July, September, and JJA. That ASMA moments/area correlations with subtropical jet latitude and altitude typically have opposite signs is consistent with the anti-correlation between jet altitude and latitude (Lorenz and DeWeaver 2007; Hartmann et al. 2013; Manney and Hegglin 2018, and references therein).

Fig. S9 also shows significant positive correlations of subtropical jet latitude with ASMA angle, strongest at 370 and 390 K in July; negative correlations with ASMA longitude and area at 350 K that are occasionally significant; and a positive correlation with ASMA longitude at 410 K in July. These are generally reflected in correlations of the opposite sign with subtropical jet altitude in Fig. S10. Figure S11 shows positive correlations of the ASMA longitude with subtropical jet core windspeed at 350 through 390 K that are significant in most or all of the reanalyses at 350 K and in June, July, and JJA at the other levels.

Correlations of ASMA area and most of the moments with the concurrent MEI index are not significant at the 95% confidence level. Figure 9 shows 350 and 390 K correlations of MEI with ASMA centroid locations, illustrating the most significant correlations. Centroid longitude correlations are consistently positive among the reanalyses at all levels, but are only significant for all three at 350 K in July (and 370 K in JJA, not shown). The most uniformly significant correlations with ENSO are for centroid latitude, which shows a consistent and generally significant anti-correlation with the MEI (the correlations at 370 / 410 K are very similar to those at 350 / 390 K). While these correlations seem at face value consistent with the ASMA / subtropical jet correlations (Fig. 9) and the negative (positive) subtropical jet latitude (altitude) correlations with ENSO shown by Manney et al. (2021, submitted to *Journal of Climate*), those jet / ENSO correlations are in fact much more significant in winter and spring than during the monsoon season, suggesting more complex relationships.

While correlations between concurrent ENSO and ASMA area are weak, Fig. 10 shows significant correlations of ASMA area with the MEI two months previously, especially in June and July (smaller but still significant correlations were found for a one-month lag at 390 and 410 K). Lag correlations for the moments and for other lags were either not significant or less significant than those for concurrent MEI. Correlations of MEI in DJF, March, April, and May with monsoon onset dates (defined as in Fig. 6) generally indicate positive but insignificant correlations with DJF and March MEI, and inconsistent results for the other months (not shown); an earlier onset date following El Niño conditions would be consistent with the positive two-month lag correlations with area (which we cannot calculate for May since the ASMA formed that early in only a few years). We note that the three years causing the late-May peak in Fig. 2 (1998, 2010, and 2016) all had El Niño conditions in the preceding March; however, several years with strong preceding El Niño conditions have late ASMA formation dates. These results add information on the complexity of the ASMA relationship to ENSO reflected in the lack of consensus in previous studies (see Section 1 for a brief review), and may support a role that has been suggested for dependence on the time of decay of El Niño in spring (e.g., Li et al. 2017; Liu et al. 2017; Hu et al. 2020).

Figure 11 shows correlations of ASMA area with the QBO, defined using 70 hPa Singapore winds (Naujokat 1986), at 390 and 410 K. Significant negative correlations with area are seen in all the reanalyses in June at 390 and 410 K (and in ERA-Interim and JRA-55 at 370 K, not shown). In September, there are significant negative correlations with the 70-hPa QBO winds in all reanalyses at 410 K (and in JRA-55 at 390 K). The moments did not in general show significant correlations with QBO, and results for QBO based on 50 hPa Singapore winds, 30–50-hPa wind shear, and lagged correlations were no more illuminating.

c. The Longer-Term Record: JRA-55

The 1958–2018 JRA-55 dataset allows us to examine a 61-year record, provided we can show that the pre-satellite and satellite period data are comparable. We assess that comparability using the JRA-55C reanalysis, which spans late 1972 through 2012 and uses only conventional data inputs. We examine four time series: JRA-55 and JRA-55C during their common period of 1973–2012; JRA-55 for 1979–2018 (the period used above for all the reanalyses); and JRA-55 for 1958–2018 (the 61-year record). Except for slightly larger areas in the 1979–2018 period at 350 and 370 K, these are all in very good agreement (e.g., Fig. S12 shows JJA-mean centroid and edge locations for these periods). Fig. 12 shows that centroid location and area at 370 K match closely in these four JRA-55/55C time series (with some day-to-day variability at the beginning and end of the season); similar congruence is seen at other levels.

Time series for the other moments, start/end dates, and duration in JRA-55 and JRA-55C exhibit similarly close agreement (not shown). With this indication of skill for these diagnostics without the inclusion of satellite data, we proceed to examine the evidence for trends in the 61-year record. As was the case for 1979–2018 (see Fig. S8), trends in the moments are generally not significant over any of the periods. Fig. 13 shows the results of the trend analysis for ASMA area at 350, 370, and 390 K, as well as for ASMA start and end dates and duration. (Area trends at 410 K resemble those at 390 K except that none are significant in JJA.) JRA-55 and JRA-55C changes are very similar for their common period. All four time series indicate significant area increases at 350 K, except for June in the early years. Area trends are significant in June through August and in JJA at 370 K and mostly not significant at the higher levels. Trends in ASMA start/end dates and duration show consistent patterns, with significant decreases (increases) in start date (end date and duration) at 350 K in all four cases and at 370 K in JRA-55 in 1979–2018 and 1958–2018 (excepting end dates for the latter), as well as largest changes in JRA-55 in the 1979–2018 period.

Increases in JRA-55 area and duration during 1979–2018 are overall larger and more significant than those in the earlier period, in JRA-55C, or in the full 61-year record. While these results are not conclusive, they do suggest the possibility of a recent acceleration in the increasing trend in ASMA area.

4. Conclusions and Discussion

We address outstanding issues regarding the climatology and variability of the Asian summer monsoon anticyclone (ASMA) using newly developed diagnostics of its moments and area. By analyzing ASMA diagnostics (analogous to those developed for the stratospheric polar vortex) on the 350 through 410 K isentropic surfaces and evaluating the robustness of our results by comparing three recent reanalyses, we provide a uniquely comprehensive synthesis of the morphology and evolution of the ASMA, assess trends in those characteristics, and examine the relationships of ASMA interannual variability to ENSO, the QBO, and the UT subtropical jet. We use the MERRA-2, ERA-Interim, and JRA-55 reanalyses for 1979–2018, extending our results to 1958–2018 using JRA-55; all of these reanalyses have been shown to be suitable for UTLS studies such as ours. Except for limited areas of disagreement as noted, our results are robust for these reanalyses.

Notable climatological characteristics of the ASMA revealed or confirmed in this study include:

- The ASMA forms slightly earlier at 350 K (late April) than at higher levels (late May / early June) and decays slightly later at 350 K (mid-October) than at higher levels (mid / late September). Its mean duration (averaged over 1979–2018 and the three reanalyses) is 120, 110, 87, and 77 days at 350, 370, 390, and 410 K, respectively.

- At its peak in July/August, the ASMA occupies $\sim$10% of the northern hemisphere.

- ASMA centroid longitudes are lowest and latitudes highest in early August when the ASMA area is largest; the ASMA thus moves westward and northward as it develops and eastward and southward as it decays.

- ASMA centroid latitude increases with height, with a climatological maximum latitude of $\sim$30°N at 350 K increasing to $\sim$37°N at 410 K; ASMA centroid longitude is similar at all levels, near 80°E at the peak of the monsoon season.

- The climatologies from the three reanalyses generally agree well at 370, 390, and 410 K, but ASMA area is larger in MERRA-2, especially at 350 K, where it exceeds that in the other reanalyses by $\sim$40–50%. This difference originates in part from a vertically localized temperature bias in MERRA-2 near 300 hPa (Gelaro et al. 2017), which may be related to differences in MERRA-2 representation of high clouds and associated heating with them (Wright et al. 2020); it is the subject of ongoing investigation.

- ASMA aspect ratios are typically between 5 and 10 when the circulation is well defined.

- The ASMA major axis is closely aligned with the latitude circle of its centroid.

- Negative values of excess kurtosis (EK) are associated with a pinched or split ASMA but are uncommon; the ASMA is on average nearly elliptical, with a slight bulge along the minor axis. Thus, although splits and bimodal structures do occur during some periods, they are not frequent or persistent enough to leave an imprint of two preferred locations in the climatology.

The northwest (southeast) motion of the ASMA during development (decay) is consistent with previous work and is thought to arise largely from seasonal changes in heating over the Iranian and Tibetan Plateaus; these changes and ASMA development also affect the location and timing of ASM rainfall onset, which in turn feeds back on ASMA development, position, and duration (e.g., Qian et al. 2002; Wu et al. 2015; Nützel et al. 2016; Wu et al. 2020). Because most studies focus on a single level, our results regarding changing ASMA position/size with height are new, though Santee et al. (2017) showed qualitatively similar evolution in a much shorter dataset.

Our results substantiate the lack of climatological bimodality in the ASMA and support and extend previous studies showing no evidence for bimodality in recent reanalyses (e.g., Ploeger et al. 2015; Nützel et al. 2016); on the other hand, infrequent brief periods of negative EK indicate that bimodality does occur in daily ASMA maps, consistent with reported shape variations (e.g., Pan et al. 2016; Honomichl and Pan 2020). The lack of climatological bimodality in centroid frequency distributions suggests that bimodality is more commonly related to shape variations than to two strongly preferred ASMA core locations, and some of the studies noted above do suggest that shape variations may be related to changes in patterns of heating and rainfall similar to those that drive the seasonal position changes. Further exploration of EK in the context of intraseasonal variability, as well as for case studies, will help quantify common shape variations of the ASMA and identify statistical patterns that arise from those shape changes; these statistical patterns can be used to explore the relationships of EK to heating and rainfall.

Previous studies that touched on ASMA area provided only qualitative results (e.g., area measured in grid-point "counts", or diagnostics of western and eastern extent; Qian et al. 2002; Liu et al. 2017; Xue et al. 2017; Xue and Chen 2019), most often based on older reanalyses such as NCEP-R1 (in which geometrical aspects of the ASMA are particularly suspect), and they typically focused on a single level, so our comprehensive assessment of ASMA area is unique.

In addition to these climatological features, the long-term reanalysis records allow us to quantify trends and interannual variability. Our trend analysis shows that:

- Significant (at the 95% confidence level) increasing trends in ASMA area over the 40-year common study period are robust among all of the reanalyses we studied (including MERRA and CFSR/CFSv2 shown in S-RIP Chapter 8, Tegtmeier et al. 2021). The area trends are not sensitive to ending years ranging from 2014 to 2018.

- Consistent with the area trends, ASMA start dates have become earlier and end dates later; consequently, its duration has increased. Area and duration trends are typically largest and most significant at 350 K and are strongest in MERRA-2. Averaged over the reanalyses, the ASMA persisted longer in 2018 than in 1979 by 44, 23, 22, and 12 days at 350, 370, 390, and 410 K, respectively.

- In the 1958–2018 JRA-55 record, trends are substantially larger and more significant for 1979–2018 than for 1958–2018 or 1973–2012, and trends are significant at the 95% confidence level at 390 and 410 K (and in many cases 370 K) only for the 1979–2018 period. Thus trends may have accelerated during the past four decades.

These trends are derived from very different metrics than those in past studies, thus providing a novel view of the changing ASMA. The trend towards earlier ASMA formation is consistent with previous work showing evidence of earlier monsoon onset using near-surface or rainfall diagnostics (Kajikawa et al. 2012; Bollasina et al. 2013; Bombardi et al. 2020, and references therein) and with previous studies suggesting earlier onset of the patterns of shifting heating rates and feedbacks with rainfall that drive the seasonal development and northwest shift of the ASMA (e.g., Ge et al. 2018a,b; Wei et al. 2019; Zhang et al. 2019; Wu et al. 2020). Until now, area trends have not been evaluated in detail and are not obviously comparable to the diverse metrics of ASMA intensity employed in prior studies. Some previous work has noted that trends in metrics of ASMA intensity may be related to long-term mean changes over a broader region in the fields (e.g., geopotential height, temperature) used to calculate those diagnostics (e.g., Xue et al. 2020). To further elucidate the proximate causes of the ASMA area and duration trends shown here, a paper in preparation explores their relationships to changes in MSF, temperature, geopotential height, tropopause variations, UT winds, and other dynamical fields; preliminary results indicate much greater complexity in the causes of these trends than a simple overall long-term increase in MSF arising from climate-change-driven increases in temperature and/or geopotential height. Given the previous work noted above suggesting that earlier ASMA onset may be related to trends in heating and rainfall, it will also be of interest to explore relationships with surface diagnostics.

Some ASMA diagnostics show robust correlations with other modes of variability:

- The ASMA centroid latitude is significantly positively (negatively) correlated with the subtropical jet core latitude (altitude).
- ASMA centroid latitude is significantly negatively correlated with concurrent ENSO.
- ASMA area is significantly positively correlated with the MEI index two months previously, particularly in June/July at 370 and 390 K.
- ASMA area is significantly negatively correlated with QBO only during June at 370, 390, and 410 K.

ENSO / ASMA centroid latitude correlations are consistent with the negative (positive) correlations of subtropical jet latitude (altitude) with ENSO shown by Manney et al. (2021). Both are in turn consistent with the climatological northward jet shift during the ASM season (e.g., Schiemann et al. 2009; Manney et al. 2014) and with the anticorrelation of jet latitude and altitude (e.g., Lorenz and DeWeaver 2007; Hartmann et al. 2013; Manney and Hegglin 2018; Manney et al. 2021). While positive lag correlations of area with ENSO seem at face value inconsistent with some previous work suggesting stronger monsoons during La Niña conditions (e.g., Tweedy et al. 2018; Yan et al. 2018), ASMA area is a very different metric than any previously employed, and our results may support suggestions in other past work linking earlier development of the ASMA to complex changes in local and remote SSTs related to the timing of decaying El Niño in spring (e.g. Li et al. 2017; Liu et al. 2017; Xue et al. 2017).

In summary, the diagnostics studied herein shed new light on interannual variability and trends in the ASMA. New insights on outstanding issues include comprehensive vertically resolved analysis of the climatology and seasonal evolution of ASMA area, position, and shape using consistently defined metrics; evidence for the lack of climatological bimodality in the ASMA; robust increasing trends in ASMA area and duration; and new results on the complex relationships of ASMA geometry and evolution to ENSO. Our results not only provide a novel view of ASMA climatology and variability, but also new tools for further exploration of ASMA dynamical and composition variability, the ability of climate models to capture this variability, and relationships of ASMA changes to surface impacts.

Acknowledgments. We thank the Microwave Limb Sounder team at JPL for computational, data processing, management, and analysis support, especially Brian W Knosp and Ryan A Fuller for data processing and management and Luis Millán for JETPAC development and operational processing; Kirstin Krüger, Susann Tegtmeier, Jonathon Wright, Matthias Nützel, Darryn Waugh, and an anonymous reviewer, for their helpful comments; and NASA's GMAO, ECMWF, and JMA for providing their assimilated data products. GLM and ZDL were partially supported by the JPL Microwave Limb Sounder team under JPL subcontracts to NWRA and NMT; GLM was also supported by a NASA Atmospheric Chemistry Modeling and Analysis project via a subcontract from JPL. KW was supported by NASA's Modeling, Analysis and Prediction (MAP) program, which also provides support for MERRA and MERRA-2. Work at the Jet Propulsion Laboratory, California Institute of Technology, was done under contract with the National Aeronautics and Space Administration. The datasets used/produced are publicly available, as follows:

- MERRA-2: https://disc.sci.gsfc.nasa.gov/uui/datasets?keywords=%22MERRA-2%22
- ERA-Interim: http://apps.ecmwf.int/datasets/
- JRA-55/JRA-55C: Through NCAR RDA at http://dx.doi.org/10.5065/D6HH6H41
- MEI: https://www.psl.noaa.gov/enso/mei.old/
- QBO: https://www.geo.fu-berlin.de/en/met/ag/strat/produkte/qbo/index.html

References

Amemiya, A., and K. Sato, 2018: A two-dimensional dynamical model for the subseasonal variability of the Asian monsoon anticyclone. *J. Atmos. Sci.*, **75 (10)**, 3597–3612, doi:10.1175/JAS-D-17-0208.1, URL https://doi.org/10.1175/JAS-D-17-0208.1, https://doi.org/10.1175/JAS-D-17-0208.1.

Bao, X., and F. Zhang, 2019: How accurate are modern atmospheric reanalyses for the data-sparse Tibetan Plateau region? *J. Clim.*, **32 (21)**, 7153–7172, doi:10.1175/JCLI-D-18-0705.1, URL https://doi.org/10.1175/JCLI-D-18-0705.1, https://doi.org/10.1175/JCLI-D-18-0705.1.

Barret, B., B. Sauvage, Y. Bennouna, and E. Le Flochmoen, 2016: Upper-tropospheric CO and O_3 budget during the Asian summer monsoon. *Atmos. Chem. Phys.*, **16 (14)**, 9129–9147, doi:10.5194/acp-16-9129-2016, URL https://www.atmos-chem-phys.net/16/9129/2016/.

Basha, G., M. V. Ratnam, and P. Kishore, 2020: Asian summer monsoon anticyclone: trends and variability. *Atmos. Chem. Phys.*, **20 (11)**, 6789–6801, doi:10.5194/acp-20-6789-2020, URL https://acp.copernicus.org/articles/20/6789/2020/.

Bergman, J. W., F. Fierli, E. J. Jensen, S. Honomichl, and L. L. Pan, 2013: Boundary layer sources for the Asian anticyclone: Regional contributions to a vertical conduit. *J. Geophys. Res.*, **118 (6)**, 2560–2575, doi:10.1002/jgrd.50142, URL https://agupubs.onlinelibrary.wiley.com/doi/abs/10.1002/jgrd.50142, https://agupubs.onlinelibrary.wiley.com/doi/pdf/10.1002/jgrd.50142.

Bloom, S. C., L. L. Takacs, A. M. da Silva, and D. Ledvina, 1996: Data assimilation using incremental analysis updates. *Mon. Weather Rev.*, **124**, 1256–1271.

Bollasina, M. A., Y. Ming, and V. Ramaswamy, 2013: Earlier onset of the Indian monsoon in the late twentieth century: The role of anthropogenic aerosols. *Geophys. Res. Lett.*, **40 (14)**, 3715–3720, doi:10.1002/grl.50719, URL https://agupubs.onlinelibrary.wiley.com/doi/abs/10.1002/grl.50719, https://agupubs.onlinelibrary.wiley.com/doi/pdf/10.1002/grl.50719.

Bollasina, M. A., Y. Ming, V. Ramaswamy, M. D. Schwarzkopf, and V. Naik, 2014: Contribution of local and remote anthropogenic aerosols to the twentieth century weakening of the South Asian Monsoon. *Geophys. Res. Lett.*, **41 (2)**, 680–687, doi:10.1002/2013GL058183, URL https://agupubs.onlinelibrary.wiley.com/doi/abs/10.1002/2013GL058183, https://agupubs.onlinelibrary.wiley.com/doi/pdf/10.1002/2013GL058183.

Bombardi, R. J., V. Moron, and J. S. Goodnight, 2020: Detection, variability, and predictability of monsoon onset and withdrawal dates: A review. *Int. J. Clim.*, **40 (2)**, 641–667, doi:10.1002/joc.6264, URL https://rmets.onlinelibrary.wiley.com/doi/abs/10.1002/joc.6264.

Boos, W. R., and T. Storelvmo, 2016: Near-linear response of mean monsoon strength to a broad range of radiative forcings. *Proceed. Natl. Acad. Sci.*, **113 (6)**, 1510–1515, doi:10.1073/pnas.1517143113, URL https://www.pnas.org/content/113/6/1510, https://www.pnas.org/content/113/6/1510.full.pdf.

Brönnimann, S., and Coauthors, 2016: Multidecadal variations of the effects of the Quasi-Biennial Oscillation on the climate system. *Atmos. Chem. Phys.*, **16 (24)**, 15 529–15 543, doi:10.5194/acp-16-15529-2016, URL https://acp.copernicus.org/articles/16/15529/2016/.

Canny, J., 1986: A computational approach to edge detection. *IEEE Transactions on Pattern Analysis and Machine Intelligence*, **PAMI-8 (6)**, 679–698, doi:10.1109/TPAMI.1986.4767851.

Chen, J., W. Huang, S. Feng, Q. Zhang, X. Kuang, J. Chen, and F. Chen, 2021: The modulation of westerlies-monsoon interaction on climate over the monsoon boundary zone in East Asia. *Intl. J. Climatol.*, **41 (S1)**, E3049–E3064, doi:https://doi.org/10.1002/joc.6903, URL https://rmets.onlinelibrary.wiley.com/doi/abs/10.1002/joc.6903, https://rmets.onlinelibrary.wiley.com/doi/pdf/10.1002/joc.6903.

Claud, C., and P. Terray, 2007: Revisiting the possible links between the quasi-biennial oscillation and the Indian summer monsoon using NCEP R-2 and CMAP fields. *J. Clim.*, **20 (5)**, 773–787, doi:10.1175/JCLI4034.1, URL https://doi.org/10.1175/JCLI4034.1, https://doi.org/10.1175/JCLI4034.1.

Dee, D. P., and Coauthors, 2011: The ERA-Interim reanalysis: configuration and performance of the data assimilation system. *Q. J. R. Meteorol. Soc.*, **137**, 553–597.

Dunkerton, T. J., 1995: Evidence of meridional motion in the summer lower stratosphere adjacent to monsoon regions. *J. Geophys. Res.*, **100 (D8)**, 16 675–16 688, doi:10.1029/95JD01263, URL https://agupubs.onlinelibrary.wiley.com/doi/abs/10.1029/95JD01263, https://agupubs.onlinelibrary.wiley.com/doi/pdf/10.1029/95JD01263.

Ebita, A., and Coauthors, 2011: The Japanese 55-year Reanalysis "JRA-55": An interim report. *SOLA*, **7**, 149–152.

Elfron, B., and R. J. Tibshirani, 1993: *An Introduction to the Bootstrap*. No. 57, Monographs on Statistics and Applied Probability, Chapman & Hall.

Fairlie, T. D., J.-P. Vernier, M. Natarajan, and K. M. Bedka, 2014: Dispersion of the Nabro volcanic plume and its relation to the Asian summer monsoon. *Atmos. Chem. Phys.*, **14**, 7045–7057.

Feba, F., K. Ashok, and M. Ravichandran, 2019: Role of changed Indo-Pacific atmospheric circulation in the recent disconnect between the Indian summer monsoon and ENSO. *Clim. Dyn.*, **52 (3)**, 1461–1470, URL https://doi.org/10.1007/s00382-018-4207-2.

Fujiwara, M., and Coauthors, 2017: Introduction to the SPARC Reanalysis Intercomparison Project (S-RIP) and overview of the reanalysis systems. *Atmos. Chem. Phys.*, **17**, 1417–1452, doi:10.5194/acp-17-1417-2017, URL www.atmos-chem-phys.net/17/1417/2017/.

Garny, H., and W. J. Randel, 2013: Dynamic variability of the Asian monsoon anticyclone observed in potential vorticity and correlations with tracer distributions. *J. Geophys. Res.*, **118 (24)**, 13,421–13,433, doi:10.1002/2013JD020908, URL https://agupubs.onlinelibrary.wiley.com/doi/abs/10.1002/2013JD020908, https://agupubs.onlinelibrary.wiley.com/doi/pdf/10.1002/2013JD020908.

Garny, H., and W. J. Randel, 2016: Transport pathways from the Asian monsoon anticyclone to the stratosphere. *Atmos. Chem. Phys.*, **16 (4)**, 2703–2718, doi:10.5194/acp-16-2703-2016, URL https://www.atmos-chem-phys.net/16/2703/2016/.

Ge, J., Q. You, and Y. Zhang, 2018a: The influence of the Asian summer monsoon onset on the northward movement of the South Asian high towards the Tibetan Plateau and its thermodynamic mechanism. *Intl. J. Climatol.*, **38 (2)**, 543–553, doi:https://doi.org/10.1002/joc.5192, URL https://rmets.onlinelibrary.wiley.com/doi/abs/10.1002/joc.5192, https://rmets.onlinelibrary.wiley.com/doi/pdf/10.1002/joc.5192.

Ge, J., Q. You, and Y. Zhang, 2018b: Interannual variation of the northward movement of the South Asian high towards the Tibetan Plateau and its relation to the Asian Summer Monsoon onset. *Atmos. Res.*, **213**, 381–388, doi:https://doi.org/10.1016/j.atmosres.2018.06.026, URL https://www.sciencedirect.com/science/article/pii/S0169809518303223.

Gelaro, R., and Coauthors, 2017: The Modern-Era Retrospective Analysis for Research and Applications, Version-2 (MERRA-2). *J. Clim.*, **30**, 5419–5454, doi:doi:10.1175/JCLI-D-16-0758.1.

Giorgetta, M. A., L. Bengtsson, and K. Arpe, 1999: An investigation of QBO signals in the east Asian and Indian monsoon in GCM experiments. *Climate Dynamics*, **15 (6)**, 435–450, URL https://doi.org/10.1007/s003820050292.

Global Modeling and Assimilation Office (GMAO), 2015: Merra-2 inst3_3d_asm_nv: 3d, 3-hourly,instantaneous, model-level, assimilation, assimilated meteorological fields v5.12.4, greenbelt, md, usa, Goddard Earth Sciences Data and Information Services Center (GES DISC), accessed 1 november 2015. doi:10.5067/WWQSXQ8IVFW8.

Hartmann, and Coauthors, 2013: *Climate Change 2013: The Physical Science Basis. Contribution of Working Group I to the Fifth Assessment Report of the Intergovernmental Panel on Climate Change*, chap. Observations: Atmosphere and Surface. Cambridge University Press, Cambridge, United Kingdom and New York, NY, USA.

Homeyer, C. R., G. L. Manney, L. F. M. A. C. Boothe, T. Xian, M. A. Olsen, M. J. Schwartz, Z. D. Lawrence, and K. Wargan, 2021: Extratropical upper troposphere and lower stratosphere (ExUTLS). *S-RIP Final Report*, M. Fujiwara, G. L. Manney, L. J. Grey, and J. S. Wright, Eds., chap. 7, in press.

Honomichl, S. B., and L. L. Pan, 2020: Transport from the Asian summer monsoon anticyclone over the western Pacific. *J. Geophys. Res.*, **125 (13)**, e2019JD032 094, doi:10.1029/2019JD032094, URL https://agupubs.onlinelibrary.wiley.com/doi/abs/10.1029/2019JD032094, e2019JD032094 2019JD032094, https://agupubs.onlinelibrary.wiley.com/doi/pdf/10.1029/2019JD032094.

Hoskins, B. J., and M. J. Rodwell, 1995: A model of the Asian summer monsoon. Part I: The global scale. *J. Atmos. Sci.*, **52 (9)**, 1329–1340, doi:10.1175/1520-0469(1995)052⟨1329:AMOTAS⟩2.0.CO;2, URL https://doi.org/10.1175/1520-0469(1995)052⟨1329:AMOTAS⟩2.0.CO;2, https://doi.org/10.1175/1520-0469(1995)052⟨1329:AMOTAS⟩2.0.CO;2.

Hrudya, P. H., H. Varikoden, R. Vishnu, and J. Kuttippurath, 2020: Changes in ENSO-monsoon relations from early to recent decades during onset, peak and withdrawal phases of Indian summer monsoon. *Climate Dynamics*, **55 (5)**, 1457–1471, URL https://doi.org/10.1007/s00382-020-05335-x.

Hsu, H.-H., C.-T. Terng, and C.-T. Chen, 1999: Evolution of large-scale circulation and heating during the first transition of Asian summer monsoon. *J. Clim.*, **12 (3)**, 793–810, doi:10.1175/1520-0442(1999)012⟨0793:EOLSCA⟩2.0.CO;2, URL https://doi.org/10.1175/1520-0442(1999)012⟨0793:EOLSCA⟩2.0.CO;2, https://doi.org/10.1175/1520-0442(1999)012⟨0793:EOLSCA⟩2.0.CO;2.

Hu, P., W. Chen, S. Chen, Y. Liu, and R. Huang, 2020: Extremely Early Summer Monsoon Onset in the South China Sea in 2019 Following an El Niño Event. *Mon. Weather Rev.*, **148 (5)**, 1877–1890, doi:10.1175/MWR-D-19-0317.1, URL https://doi.org/10.1175/MWR-D-19-0317.1, https://journals.ametsoc.org/mwr/article-pdf/148/5/1877/4928037/mwrd190317.pdf.

Ju, J., and J. Slingo, 1995: The Asian summer monsoon and ENSO. *Q. J. R. Meteorol. Soc.*, **121 (525)**, 1133–1168, doi:10.1002/qj.49712152509, URL https://rmets.onlinelibrary.wiley.com/doi/abs/10.1002/qj.49712152509, https://rmets.onlinelibrary.wiley.com/doi/pdf/10.1002/qj.49712152509.

Kajikawa, Y., T. Yasunari, S. Yoshida, and H. Fujinami, 2012: Advanced Asian summer monsoon onset in recent decades. *Geophys. Res. Lett.*, **39 (3)**, doi:10.1029/2011GL050540, URL https://agupubs.onlinelibrary.wiley.com/doi/abs/10.1029/2011GL050540, https://agupubs.onlinelibrary.wiley.com/doi/pdf/10.1029/2011GL050540.

Kelly, P., L. R. Leung, K. Balaguru, W. Xu, B. Mapes, and B. Soden, 2018: Shape of Atlantic tropical cyclone tracks and the Indian monsoon. *Geophys. Res. Lett.*, **45 (19)**, 10,746–10,755, doi:10.1029/2018GL080098, URL https://agupubs.onlinelibrary.wiley.com/doi/abs/10.1029/2018GL080098, https://agupubs.onlinelibrary.wiley.com/doi/pdf/10.1029/2018GL080098.

Kobayashi, C. A., H. Endo, Y. Ota, C. Kobayashi, H. Onoda, Y. Harada, K. Onogi, and H. Kamahori, 2014: Preliminary results of the JRA-55C, an atmospheric reanalysis assimilating conventional observations only. *Sci. Online Lett. Atmos.*, **10**, 78–82.

Kobayashi, S., and Coauthors, 2015: The JRA-55 reanalysis: General specification and basic characteristics. *J. Meteor. Soc. Japan*, **93**, doi:10.2151/jmsj.2015-001.

Kodera, K., N. Eguchi, R. Ueyama, Y. Kuroda, C. Kobayashi, B. M. Funatsu, and C. Claud, 2019: Implication of tropical lower stratospheric cooling in recent trends in tropical circulation and deep convective activity. *Atmos. Chem. Phys.*, **19 (4)**, 2655–2669, doi:10.5194/acp-19-2655-2019, URL https://www.atmos-chem-phys.net/19/2655/2019/.

Lawrence, Z. D., and G. L. Manney, 2018: Characterizing stratospheric polar vortex variability with computer vision techniques. *Journal of Geophysical Research: Atmospheres*, **123 (3)**, 1510–1535, doi:10.1002/2017JD027556, URL http://dx.doi.org/10.1002/2017JD027556, 2017JD027556.

Lawrence, Z. D., and G. L. Manney, 2020: Does the Arctic Stratospheric Polar Vortex Exhibit Signs of Preconditioning Prior to Sudden Stratospheric Warmings? *J. Atmos. Sci.*, **77 (2)**, 611–632, doi:10.1175/JAS-D-19-0168.1, URL https://doi.org/10.1175/JAS-D-19-0168.1, https://journals.ametsoc.org/jas/article-pdf/77/2/611/4917744/jas-d-19-0168_1.pdf.

Lawrence, Z. D., G. L. Manney, and K. Wargan, 2018: Reanalysis intercomparisons of stratospheric polar processing diagnostics. *Atmos. Chem. Phys.*, **18**, 13 547–13 579, doi:10.5194/acp-18-13547-2018.

Li, T., B. Wang, B. Wu, T. Zhou, C.-P. Chang, and R. Zhang, 2017: Theories on formation of an anomalous anticyclone in western North Pacific during El Niño: A review. *J. Meteorol. Res.*, **31 (6)**, 987–1006, URL https://doi.org/10.1007/s13351-017-7147-6.

Li, Y., N.-C. Lau, C.-Y. Tam, H.-N. Cheung, Y. Deng, and H. Zhang, 2021: Projected changes in the characteristics of the East Asian summer monsoonal front and their impacts on the regional precipitation. *Clim. Dyn.*, **56 (11)**, 4013–4026, URL https://doi.org/10.1007/s00382-021-05687-y.

Liu, B., G. Wu, J. Mao, and J. He, 2013: Genesis of the South Asian high and its impact on the Asian summer monsoon onset. *J. Clim.*, **26 (9)**, 2976–2991, doi:10.1175/JCLI-D-12-00286.1, URL https://journals.ametsoc.org/view/journals/clim/26/9/jcli-d-12-00286.1.xml.

Liu, B., C. Zhu, and Y. Yuan, 2017: Two interannual dominant modes of the South Asian High in May and their linkage to the tropical SST anomalies. *Clim. Dyn.*, **49 (7)**, 2705–2720, URL https://doi.org/10.1007/s00382-016-3490-z.

Liu, Y., B. Hoskins, and M. Blackburn, 2007: Impact of Tibetan orography and heating on the summer flow over Asia. *J. Meteorol. Soc. Japan*, **85B**, 1–19, doi:10.2151/jmsj.85B.1.

Liu, Y., G. Wu, and R. Ren, 2004: Relationship between the subtropical anticyclone and diabatic heating. *J. Clim.*, **17 (4)**, 682–698, doi:10.1175/1520-0442(2004)017⟨0682:RBTSAA⟩2.0.CO;2, URL https://journals.ametsoc.org/view/journals/clim/17/4/1520-0442_2004_017_0682_rbtsaa_2.0.co_2.xml.

Long, C. S., M. Fujiwara, S. Davis, D. M. Mitchell, and C. J. Wright, 2017: Climatology and interannual variability of dynamic variables in multiple reanalyses evaluated by the SPARC Reanalysis Intercomparison Project (S-RIP). *Atmos. Chem. Phys.*, **17**, 14,593–14,629, URL https://doi.org/10.5194/acp-17-14593-2017.

Lorenz, D. J., and E. T. DeWeaver, 2007: Tropopause height and zonal wind response to global warming in the IPCC scenario integrations. *J. Geophys. Res.*, **112**, D10119, doi:10.1029/2006JD008087.

Manney, G. L., and M. I. Hegglin, 2018: Seasonal and regional variations in long-term changes in upper tropospheric jets from reanalyses. *J. Clim.*, **31**, 423–448.

Manney, G. L., M. I. Hegglin, W. H. Daffer, M. J. Schwartz, M. L. Santee, and S. Pawson, 2014: Climatology of upper tropospheric/lower stratospheric (UTLS) jets and tropopauses in MERRA. *J. Clim.*, **27**, 3248–3271.

Manney, G. L., M. I. Hegglin, and Z. D. Lawrence, 2021: Seasonal and regional signatures of ENSO in upper tropospheric jets characteristics from reanalyses, *J. Clim., submitted*.

Manney, G. L., K. Krüger, J. L. Sabutis, S. A. Sena, and S. Pawson, 2005a: The remarkable 2003-2004 winter and other recent warm winters in the Arctic stratosphere since the late 1990s. *J. Geophys. Res.*, **110**, D04107, doi:10.1029/2004JD005367.

Manney, G. L., and Z. D. Lawrence, 2016: The major stratospheric final warming in 2016: dispersal of vortex air and termination of Arctic chemical ozone loss. *Atmos. Chem. Phys.*, **16 (23)**, 15 371–15 396, doi:10.5194/acp-16-15371-2016, URL https://www.atmos-chem-phys.net/16/15371/2016/.

Manney, G. L., J. L. Sabutis, S. Pawson, M. L. Santee, B. Naujokat, R. Swinbank, M. E. Gelman, and W. Ebisuzaki, 2003: Lower stratospheric temperature differences between meteorological analyses in two cold Arctic winters and their impact on polar processing studies. *J. Geophys. Res.*, **108**, 8328, doi:10.1029/2001JD001149.

Manney, G. L., and Coauthors, 2005b: Diagnostic comparison of meteorological analyses during the 2002 Antarctic winter. *Mon. Weather Rev.*, **133**, 1261–1278.

Manney, G. L., and Coauthors, 2011a: Jet characterization in the upper troposphere/lower stratosphere (UTLS): Applications to climatology and transport studies. *Atmos. Chem. Phys.*, **11**, 6115–6137.

Manney, G. L., and Coauthors, 2011b: Unprecedented Arctic ozone loss in 2011. *Nature*, **478**, 469–475.

Manney, G. L., and Coauthors, 2017: Reanalysis comparisons of upper tropospheric/lower stratospheric jets and multiple tropopauses. *Atmos. Chem. Phys.*, 11 541–11 566.

Matthewman, N. J., and J. G. Esler, 2011: Stratospheric sudden warmings as self-tuning resonances. Part I: Vortex splitting events. *J. Atmos. Sci.*, **68 (11)**, 2481–2504, doi:10.1175/JAS-D-11-07.1, URL https://doi.org/10.1175/JAS-D-11-07.1, https://doi.org/10.1175/JAS-D-11-07.1.

Matthewman, N. J., J. G. Esler, A. J. Charlton-Perez, and L. M. Polvani, 2009: A new look at stratospheric sudden warmings. Part III: Polar vortex evolution and vertical structure. *J. Clim.*, **22**, 1566–1585.

Mitchell, D. M., A. J. Charlton-Perez, and L. J. Gray, 2011: Characterizing the variability and extremes of the stratospheric polar vortices using 2d moment analysis. *J. Atmos. Sci.*, **68**, 1194–1213.

Mukherjee, B. K., K. Indira, R. S. Reddy, and B. V. Ramana Murty, 1985: Quasi-Biennial Oscillation in Stratospheric Zonal Wind and Indian Summer Monsoon. *Mon. Weather Rev.*, **113 (8)**, 1421–1424, doi:10.1175/1520-0493(1985)113⟨1421:QBOISZ⟩2.0.CO;2, URL https://doi.org/10.1175/1520-0493(1985)113⟨1421:QBOISZ⟩2.0.CO;2, https://journals.ametsoc.org/mwr/article-pdf/113/8/1421/4168836/1520-0493(1985)113_1421_qboisz_2_0_co_2.pdf.

Naujokat, B., 1986: An update of the observed quasi-biennial oscillation of the stratospheric winds over the tropics. *J. Atmos. Sci.*, **43 (17)**, 1873–1877, doi:10.1175/1520-0469(1986)043⟨1873:AUOTOQ⟩2.0.CO;2, URL https://doi.org/10.1175/1520-0469(1986)043⟨1873:AUOTOQ⟩2.0.CO;2, https://doi.org/10.1175/1520-0469(1986)043⟨1873:AUOTOQ⟩2.0.CO;2.

Nützel, M., M. Dameris, and H. Garny, 2016: Movement, drivers and bimodality of the south Asian high. *Atmos. Chem. Phys.*, **16**, 14,755–14,774.

Nützel, M., A. Podglajen, H. Garny, and F. Ploeger, 2019: Quantification of water vapour transport from the Asian monsoon to the stratosphere. *Atmos. Chem. Phys.*, **19 (13)**, 8947–8966, doi:10.5194/acp-19-8947-2019, URL https://www.atmos-chem-phys.net/19/8947/2019/.

Oliver, E. C. J., 2016: Blind use of reanalysis data: apparent trends in Madden-Julian Oscillation activity driven by observational changes. *Intl. J. Clim.*, **36**, 3458–3468, doi:10.1002/joc.4568, URL http://dx.doi.org/10.1002/joc.4568.

Pan, L. L., S. B. Honomichl, D. E. Kinnison, M. Abalos, W. J. Randel, J. W. Bergman, and J. Bian, 2016: Transport of chemical tracers from the boundary layer to stratosphere associated with the dynamics of the Asian summer monsoon. *J. Geophys. Res.*, **121 (23)**, 14,159–14,174, doi:10.1002/2016JD025616, URL https://agupubs.onlinelibrary.wiley.com/doi/abs/10.1002/2016JD025616, https://agupubs.onlinelibrary.wiley.com/doi/pdf/10.1002/2016JD025616.

Pawson, S., and M. Fiorino, 1998: A comparison of reanalyses in the tropical stratosphere. Part 1: thermal structure and the annual cycle. *Clim. Dyn.*, **14 (9)**, 631–644, doi:10.1007/s003820050246, URL https://doi.org/10.1007/s003820050246.

Ploeger, F., and Coauthors, 2015: A potential vorticity-based determination of the transport barrier in the Asian summer monsoon anticyclone. *Atmos. Chem. Phys.*, **15 (22)**, 13 145–13 159, doi:10.5194/acp-15-13145-2015, URL https://www.atmos-chem-phys.net/15/13145/2015/.

Popovic, J. M., and R. A. Plumb, 2001: Eddy Shedding from the Upper-Tropospheric Asian Monsoon Anticyclone. *J. Atmos. Sci.*, **58 (1)**, 93–104, doi:10.1175/1520-0469(2001)058⟨0093:ESFTUT⟩2.0.CO;2, URL https://doi.org/10.1175/1520-0469(2001)058⟨0093:ESFTUT⟩2.0.CO;2, https://journals.ametsoc.org/jas/article-pdf/58/1/93/3452142/1520-0469(2001)058_0093_esftut_2_0_co_2.pdf.

Preethi, B., M. Mujumdar, R. H. Kripalani, A. Prabhu, and R. Krishnan, 2017: Recent trends and tele-connections among south and east Asian summer monsoons in a warming environment. *Clim. Dyn.*, **48 (7)**, 2489–2505, doi:10.1007/s00382-016-3218-0, URL https://doi.org/10.1007/s00382-016-3218-0.

Qian, Y., Q. Zhang, Y. Yao, and X. Zhang, 2002: Seasonal variation and heat preference of the south Asia high. *Adv. Atmos. Sci.*, **19 (5)**, 821–836, doi:10.1007/s00376-002-0047-3, URL https://doi.org/10.1007/s00376-002-0047-3.

Randel, W. J., and M. Park, 2006: Deep convective influence on the Asian summer monsoon anticyclone and associated tracer variability observed with Atmospheric Infrared Sounder (AIRS). *J. Geophys. Res.*, **111 (D12)**, doi:10.1029/2005JD006490, URL https://agupubs.onlinelibrary.wiley.com/doi/abs/10.1029/2005JD006490, https://agupubs.onlinelibrary.wiley.com/doi/pdf/10.1029/2005JD006490.

Randel, W. J., F. Wu, and D. J. Gaffen, 2000: Interannual variability of the tropical tropopause derived from radiosonde data and NCEP reanalyses. *J. Geophys. Res.*, **105**, 15,509–15,523.

RavindraBabu, S., M. Venkat Ratnam, G. Basha, and B. Krishnamurthy, 2019: Indian summer monsoon onset signatures on the tropical tropopause layer. *Atmos. Sci. Lett.*, **20 (3)**, e884, doi:10.1002/asl.884, URL https://rmets.onlinelibrary.wiley.com/doi/abs/10.1002/asl.884, https://rmets.onlinelibrary.wiley.com/doi/pdf/10.1002/asl.884.

Ren, R., C. Zhu, and M. Cai, 2019: Linking quasi-biweekly variability of the south Asian high to atmospheric heating over Tibetan Plateau in summer. *Clim. Dyn.*, **53 (5)**, 3419–3429, doi:10.1007/s00382-019-04713-4, URL https://doi.org/10.1007/s00382-019-04713-4.

Samanta, D., B. Rajagopalan, K. B. Karnauskas, L. Zhang, and N. F. Goodkin, 2020: La Niña's diminishing fingerprint on the central Indian summer monsoon. *Geophys. Res. Lett.*, **47 (2)**, e2019GL086 237, doi:10.1029/2019GL086237, URL https://agupubs.onlinelibrary.wiley.com/doi/abs/10.1029/2019GL086237, https://agupubs.onlinelibrary.wiley.com/doi/pdf/10.1029/2019GL086237.

Santee, M. L., G. L. Manney, N. J. Livesey, M. J. Schwartz, J. L. Neu, and W. G. Read, 2017: A comprehensive overview of the climatological composition of the Asian summer monsoon anticyclone based on 10 years of Aura Microwave Limb Sounder measurements. *J. Geophys. Res.*, **122**, 5491–5514, doi:10.1002/2016JD026408, URL http://dx.doi.org/10.1002/2016JD026408.

Schiemann, R., D. Lüthi, and C. Schar, 2009: Seasonality and interannual variability of the westerly jet in the Tibetan Plateau region. *J. Clim.*, **22**, 2940–2957.

Seetha, C. J., H. Varikoden, C. A. Babu, and J. Kuttippurath, 2020: Significant changes in the ENSO-monsoon relationship and associated circulation features on multidecadal timescale. *Clim. Dyn.*, **54 (3)**, 1491–1506, URL https://doi.org/10.1007/s00382-019-05071-x.

Shi, C., Y. Huang, D. Guo, S. Zhou, K. Hu, and Y. Liu, 2018: Comparison of trends and abrupt changes of the South Asia high from 1979 to 2014 in reanalysis and radiosonde datasets. *J. Atmos. Solar-Terrest. Phys.*, **170**, 48–54, doi:https://doi.org/10.1016/j.jastp.2018.02.005, URL https://www.sciencedirect.com/science/article/pii/S1364682617304650.

Tegtmeier, S., and Coauthors, 2020: Temperature and tropopause characteristics from reanalyses data in the tropical tropopause layer. *Atmos. Chem. Phys.*, **20 (2)**, 753–770, doi:10.5194/acp-20-753-2020, URL https://www.atmos-chem-phys.net/20/753/2020/.

Tegtmeier, S., and Coauthors, 2021: Tropical troposphere layer. *S-RIP Final Report*, M. Fujiwara, G. L. Manney, L. J. Grey, and J. S. Wright, Eds., chap. 8, in press.

Tweedy, O. V., D. W. Waugh, W. J. Randel, M. Abalos, L. D. Oman, and D. E. Kinnison, 2018: The impact of Boreal summer ENSO events on tropical lower stratospheric ozone. *J. Geophys. Res.*, **123 (17)**, 9843–9857, doi:10.1029/2018JD029020, URL https://agupubs.onlinelibrary.wiley.com/doi/abs/10.1029/2018JD029020, https://agupubs.onlinelibrary.wiley.com/doi/pdf/10.1029/2018JD029020.

Vogel, B., and Coauthors, 2016: Long-range transport pathways of tropospheric source gases originating in Asia into the northern lower stratosphere during the Asian monsoon season 2012. *Atmos. Chem. Phys.*, **16**, 15 301–15 325, doi:10.5194/acp-16-15301-2016.

Wang, B., R. Wu, and K.-M. Lau, 2001: Interannual Variability of the Asian Summer Monsoon: Contrasts between the Indian and the Western North Pacific–East Asian Monsoons*. *J. Clim.*, **14 (20)**, 4073–4090, doi:10.1175/1520-0442(2001)014⟨4073:IVOTAS⟩2.0.CO;2, URL https://doi.org/10.1175/1520-0442(2001)014⟨4073:IVOTAS⟩2.0.CO;2, https://journals.ametsoc.org/jcli/article-pdf/14/20/4073/3768288/1520-0442(2001)014_4073_ivotas_2_0_co_2.pdf.

Wang, L., A. Dai, S. Guo, and J. Ge, 2017: Establishment of the South Asian high over the Indo-China Peninsula during late spring to summer. *Advances. Atmos. Sci.*, **34 (2)**, 169–180, URL https://doi.org/10.1007/s00376-016-6061-7.

Wang, X., X. Jiang, S. Yang, and Y. Li, 2013: Different impacts of the two types of El Niño on Asian summer monsoon onset. *Env. Res. Lett.*, **8 (4)**, 044 053, doi:10.1088/1748-9326/8/4/044053, URL https://doi.org/10.1088%2F1748-9326%2F8%2F4%2F044053.

Waugh, D. W., and W. J. Randel, 1999: Climatology of Arctic and Antarctic polar vortices using elliptical diagnostics. *J. Atmos. Sci.*, **56**, 1594–1613.

Webster, P. J., V. O. Magaña, T. N. Palmer, J. Shukla, R. A. Tomas, M. Yanai, and T. Yasunari, 1998: Monsoons: Processes, predictability, and the prospects for prediction. *J. Geophys. Res.*, **103 (C7)**, 14 451–14 510, doi:10.1029/97JC02719, URL https://agupubs.onlinelibrary.wiley.com/doi/abs/10.1029/97JC02719, https://agupubs.onlinelibrary.wiley.com/doi/pdf/10.1029/97JC02719.

Wei, W., R. Zhang, S. Yang, W. Li, and M. Wen, 2019: Quasi-biweekly oscillation of the South Asian High and its role in connecting the Indian and East Asian summer rainfalls. *Geophys. Res. Lett.*, **46 (24)**, 14 742–14 750, doi:https://doi.org/10.1029/2019GL086180, URL https://agupubs.onlinelibrary.wiley.com/doi/abs/10.1029/2019GL086180, https://agupubs.onlinelibrary.wiley.com/doi/pdf/10.1029/2019GL086180.

Wilks, D. S., 2011: *Statistical Methods in the Atmospheric Sciences*. 3rd ed., Elsevier Academic Press, volume 100, International Geophysics Series.

Wolter, K., and M. S. Timlin, 2011: El Niño/Southern Oscillation behaviour since 1871 as diagnosed in an extended multivariate ENSO index (MEI.ext). *Intl. J. Clim.*, **31**, 1074–1087, doi:10.1002/joc.2336, URL http://dx.doi.org/10.1002/joc.2336.

Wright, J. S., and Coauthors, 2020: Differences in tropical high clouds among reanalyses: origins and radiative impacts. *Atmos. Chem. Phys.*, **20 (14)**, 8989–9030, doi:10.5194/acp-20-8989-2020, URL https://acp.copernicus.org/articles/20/8989/2020/.

Wu, C.-H., P.-C. Tsai, and N. Freychet, 2020: Changing dynamical control of early Asian summer monsoon in the mid-1990s. *Clim. Dyn.*, **54 (1)**, 85–98, URL https://doi.org/10.1007/s00382-019-04989-6.

Wu, G., B. He, Y. Liu, Q. Bao, and R. Ren, 2015: Location and variation of the summertime upper-troposphere temperature maximum over South Asia. *Clim. Dyn.*, **45 (9)**, 2757–2774, URL https://doi.org/10.1007/s00382-015-2506-4.

Wu, L., X. Feng, and M. Liang, 2017: Insensitivity of the Summer South Asian High Intensity to a Warming Tibetan Plateau in Modern Reanalysis Datasets. *J. Clim.*, **30 (8)**, 3009–3024, doi:10.1175/JCLI-D-16-0359.1, URL https://doi.org/10.1175/JCLI-D-16-0359.1, https://journals.ametsoc.org/jcli/article-pdf/30/8/3009/4082806/jcli-d-16-0359_1.pdf.

Xian, T., and C. R. Homeyer, 2019: Global tropopause altitudes in radiosondes and reanalyses. *Atmos. Chem. Phys.*, **19**, 5661–5678.

Xue, X., and W. Chen, 2019: Distinguishing interannual variations and possible impacted factors for the northern and southern mode of South Asia High. *Clim. Dyn.*, **53 (7)**, 4937–4959, URL https://doi.org/10.1007/s00382-019-04837-7.

Xue, X., W. Chen, and S. Chen, 2017: The climatology and interannual variability of the South Asia high and its relationship with ENSO in CMIP5 models. *Clim. Dyn.*, **48 (11)**, 3507–3528, URL https://doi.org/10.1007/s00382-016-3281-6.

Xue, X., W. Chen, and S. Hou, 2020: The long-term variation in the South Asia High intensity measured by 150-hpa eddy geopotential height. *Meteorol. and Atmos. Phys.*, **132 (6)**, 833–844, URL https://doi.org/10.1007/s00703-020-00723-8.

Yan, R.-C., J.-C. Bian, and Q.-J. Fan, 2011: The impact of the south Asia high bimodality on the chemical composition of the upper troposphere and lower stratosphere. *Atmos. Ocean. Sci. Lett.*, **4 (4)**, 229–234, doi:10.1080/16742834.2011.11446934, URL https://doi.org/10.1080/16742834.2011.11446934, https://doi.org/10.1080/16742834.2011.11446934.

Yan, X., P. Konopka, F. Ploeger, A. Podglajen, J. S. Wright, R. Müller, and M. Riese, 2019: The efficiency of transport into the stratosphere via the Asian and North American summer monsoon circulations. *Atmos. Chem. Phys.*, **19 (24)**, 15 629–15 649, doi:10.5194/acp-19-15629-2019, URL https://www.atmos-chem-phys.net/19/15629/2019/.

Yan, X., P. Konopka, F. Ploeger, M. Tao, R. Müller, M. L. Santee, J. Bian, and M. Riese, 2018: El Niño Southern Oscillation influence on the Asian summer monsoon anticyclone. *Atmos. Chem. Phys.*, **18 (11)**, 8079–8096, doi:10.5194/acp-18-8079-2018, URL https://www.atmos-chem-phys.net/18/8079/2018/.

Yang, S., Z. Wei, B. Chen, and X. Xu, 2020: Influences of atmospheric ventilation on the composition of the upper troposphere and lower stratosphere during the two primary modes of the South Asia high. *Meteorol. Atmos. Phys.*, **132 (4)**, 559–570, URL https://doi.org/10.1007/s00703-019-00706-4.

Yuan, Y., and S. Yang, 2012: Impacts of different types of El Niño on the east Asian climate: Focus on ENSO cycles. *J. Clim.*, **25 (21)**, 7702–7722, doi:10.1175/JCLI-D-11-00576.1, URL https://doi.org/10.1175/JCLI-D-11-00576.1, https://journals.ametsoc.org/jcli/article-pdf/25/21/7702/4005459/jcli-d-11-00576_1.pdf.

Zarrin, A., H. Ghaemi, M. Azadi, and M. Farajzadeh, 2010: The spatial pattern of summertime subtropical anticyclones over Asia and Africa: A climatological review. *Intl. J. Clim.*, **30 (2)**, 159–173, doi:10.1002/joc.1879, URL https://rmets.onlinelibrary.wiley.com/doi/abs/10.1002/joc.1879, https://rmets.onlinelibrary.wiley.com/doi/pdf/10.1002/joc.1879.

Zhang, K., R. Fu, T. Wang, and Y. Liu, 2016: Impact of geographic variations of the convective and dehydration center on stratospheric water vapor over the Asian monsoon region. *Atmos. Chemistry. Phys.*, **16 (12)**, 7825–7835, doi:10.5194/acp-16-7825-2016, URL https://www.atmos-chem-phys.net/16/7825/2016/.

Zhang, K., T. Wang, M. Xu, and J. Zhang, 2019: Influence of wintertime polar vortex variation on the climate over the north pacific during late winter and spring. *Atmosphere*, **10 (11)**, URL https://www.mdpi.com/2073-4433/10/11/670.

Zhang, Q., G. Wu, and Y. Qian, 2002: The bimodality of the 100 hPa south Asia high and its relationship to the climate anomaly over east Asia in summer. *J. Meteor. Soc. Japan*, **80 (4)**, 733–744, doi:10.2151/jmsj.80.733.

Zhou, N., Y. Yu, and Y. Qian, 2009: Bimodality of the South Asia High simulated by coupled models. *Adv. Atmos. Sci.*, **26 (6)**, 1226, doi:10.1007/s00376-009-7219-3, URL https://doi.org/10.1007/s00376-009-7219-3.

Zhu, Q., Y. Liu, T. Shao, R. Luo, and Z. Tan, 2021: Role of the Tibetan Plateau in northern drought induced by changes in the subtropical westerly jet. *J. Clim.*, **34 (12)**, 4955–4969, doi:10.1175/JCLI-D-20-0799.1, URL https://journals.ametsoc.org/view/journals/clim/34/12/JCLI-D-20-0799.1.xml.

LIST OF FIGURES

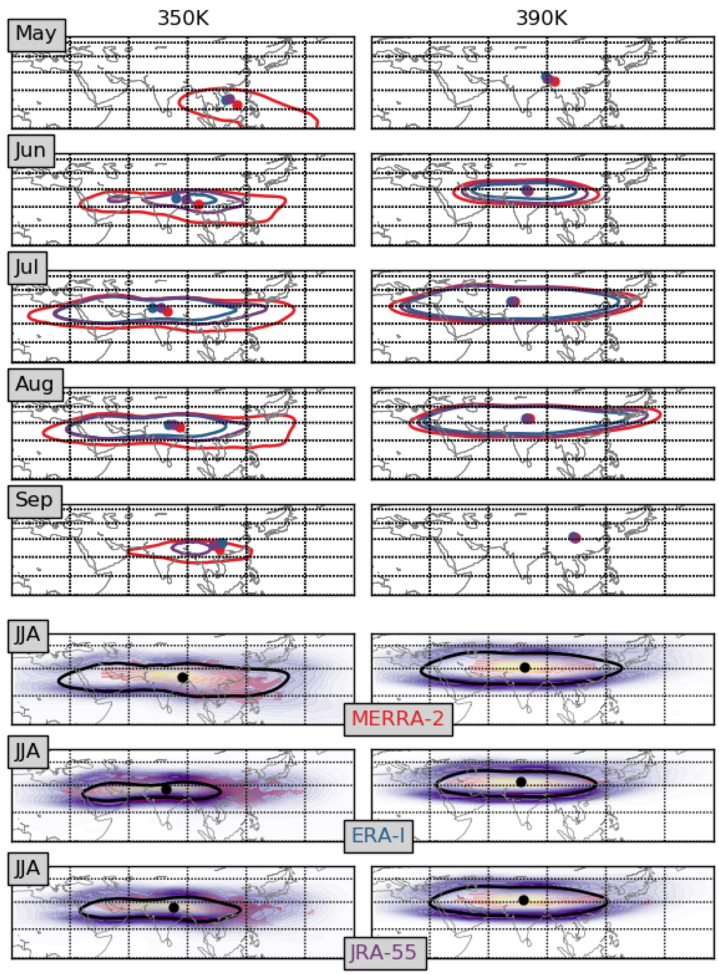

1135 FIG. 1. (Top five rows) Climatological mean (1979 through 2018) ASMA edge and centroid locations at 350 K
1136 and 390 K for May through October, and MERRA-2 (red), ERA-Interim (blue), and JRA-55 (purple). (Bottom
1137 three rows) frequency distributions of ASMA edge (purples) and centroid (reds/oranges) locations at 350 K and
1138 390 K for JJA, from (top to bottom) MERRA-2, ERA-Interim, and JRA-55. Maps are shown in the cylindrical
1139 equal area projection used to calculate the moments. The longitude domain is 0 to 180°E, with dashed lines
1140 every 30°; the latitude domain is 0 to 60°N, with dashed lines every 15°.

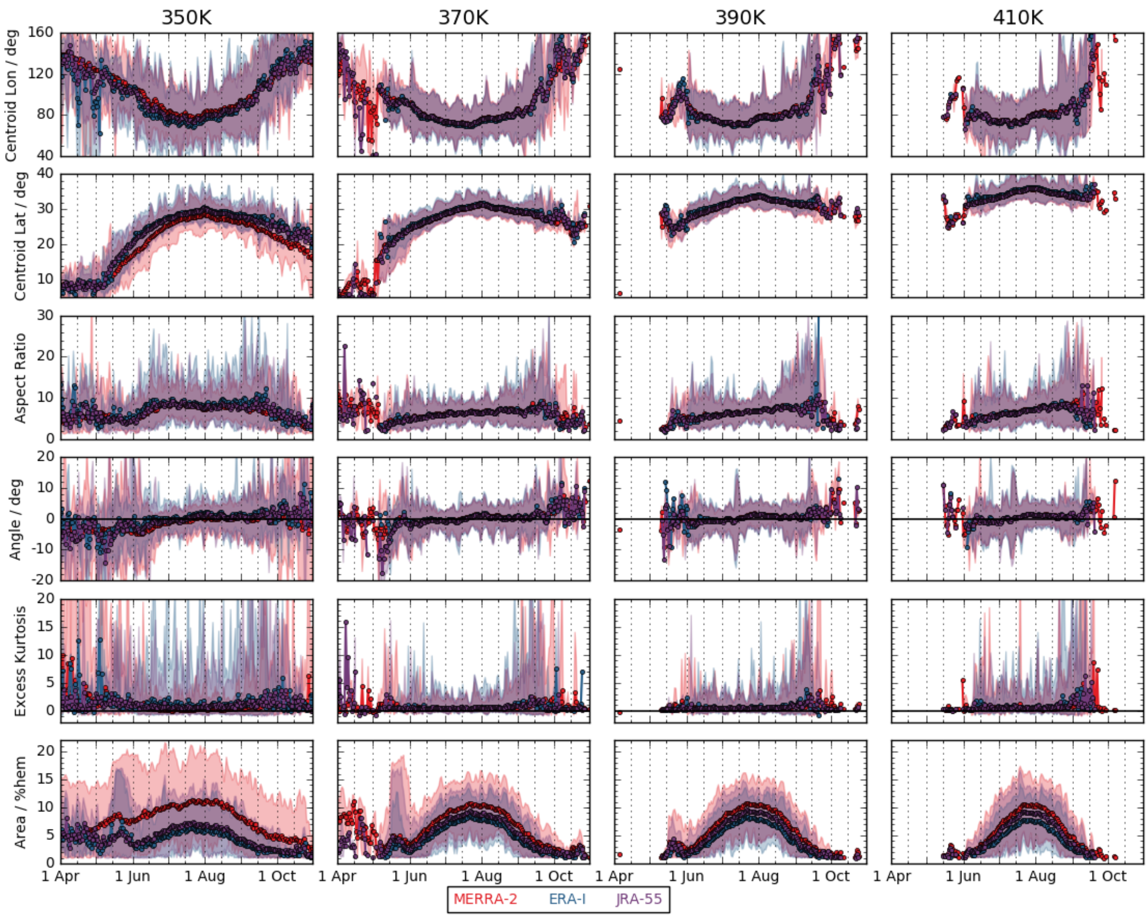

FIG. 2. Climatological (1979–2018) time series of moments and area of the ASMA at (left to right) 350, 370, 390, and 410 K; fields are top to bottom: centroid longitude, centroid latitude, aspect ratio, angle, excess kurtosis, and area. Envelopes show the range of values for the corresponding reanalysis (colors are shown in the legend).

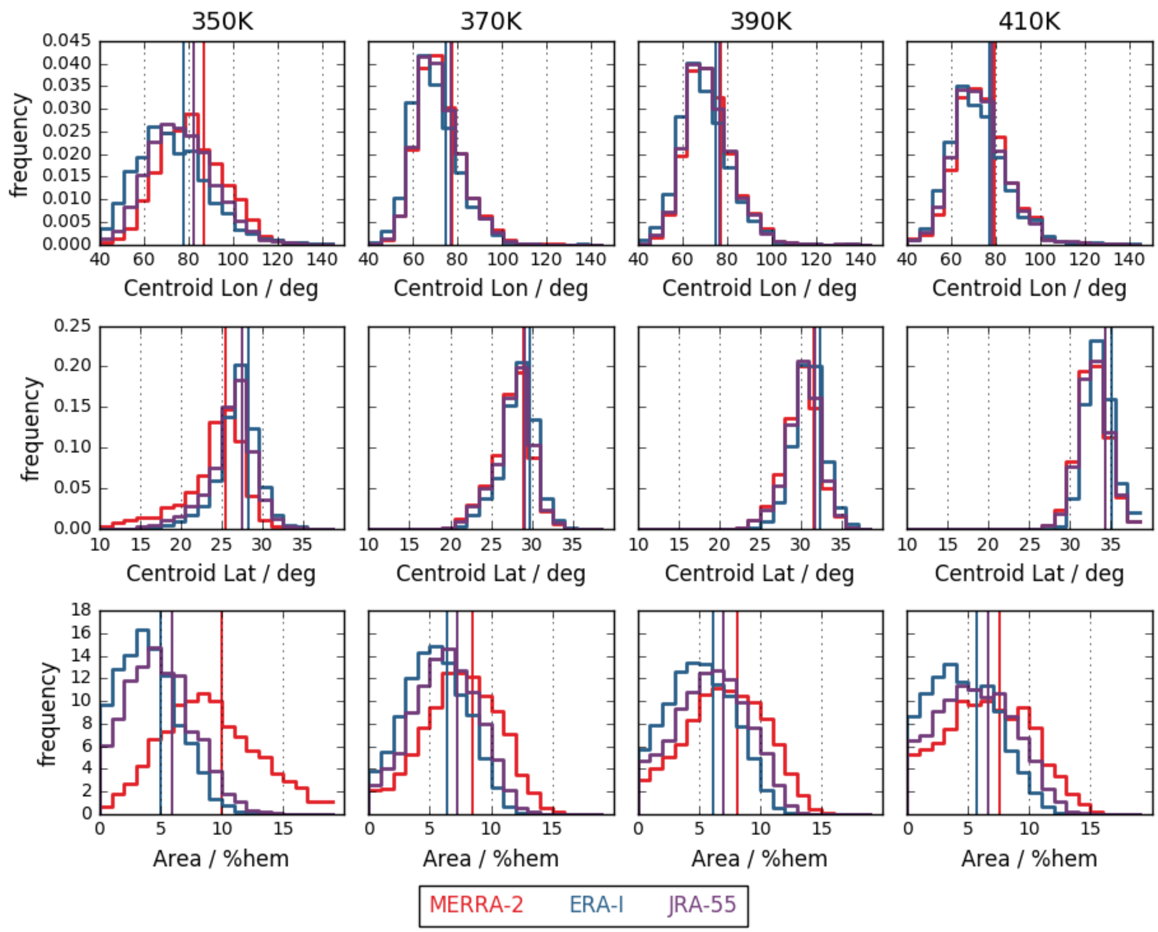

FIG. 3. Histograms of climatological JJA ASMA centroid locations and area (see Fig. S6 for aspect ratio and angle histograms). Vertical lines show climatological mean for each reanalysis.

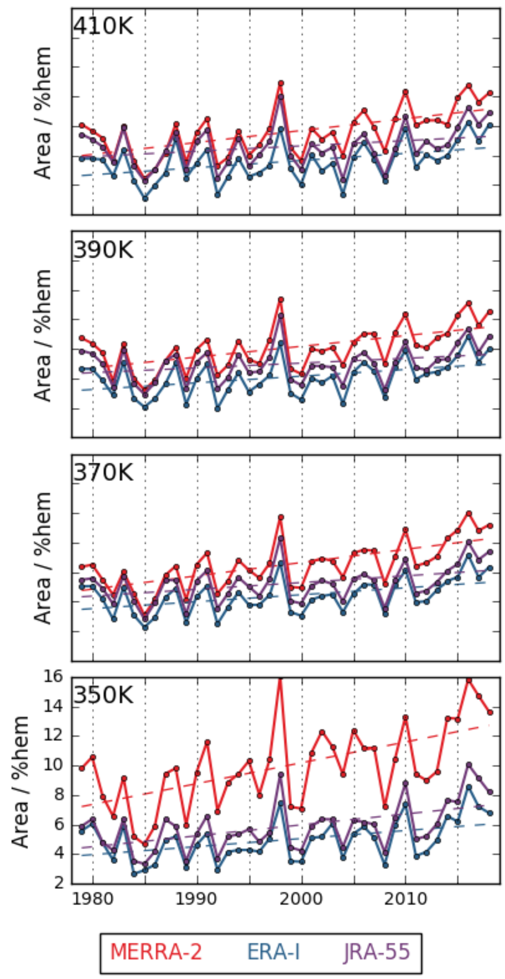

1147 FIG. 4. Time series for 1979 through 2018 of JJA ASMA area at (bottom to top) 350, 370, 390, and 410 K for
1148 the three reanalyses. Overlaid dashed lines show linear fits to the values. See Fig. S7 for moments timeseries.

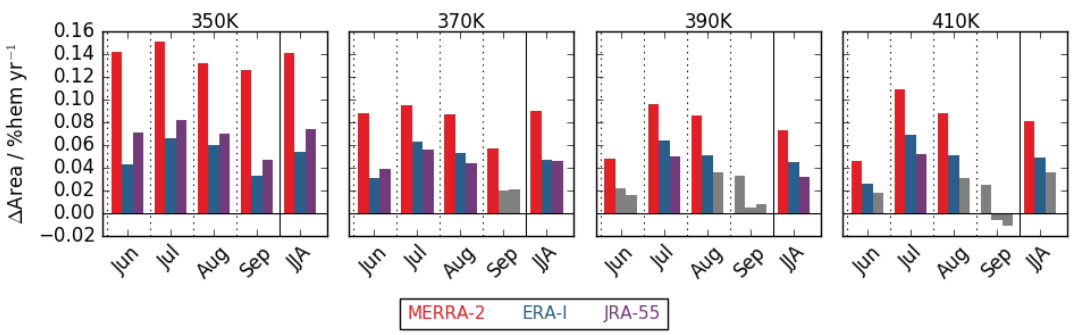

FIG. 5. Slopes of linear fits to the ASMA area time series shown in Figure 4. Bars in the reanalysis colors indicate slopes that are significant at the 95% confidence level based on a permutation analysis (see Section 2b). Fig. S8 shows a similar analysis for ASMA moments.

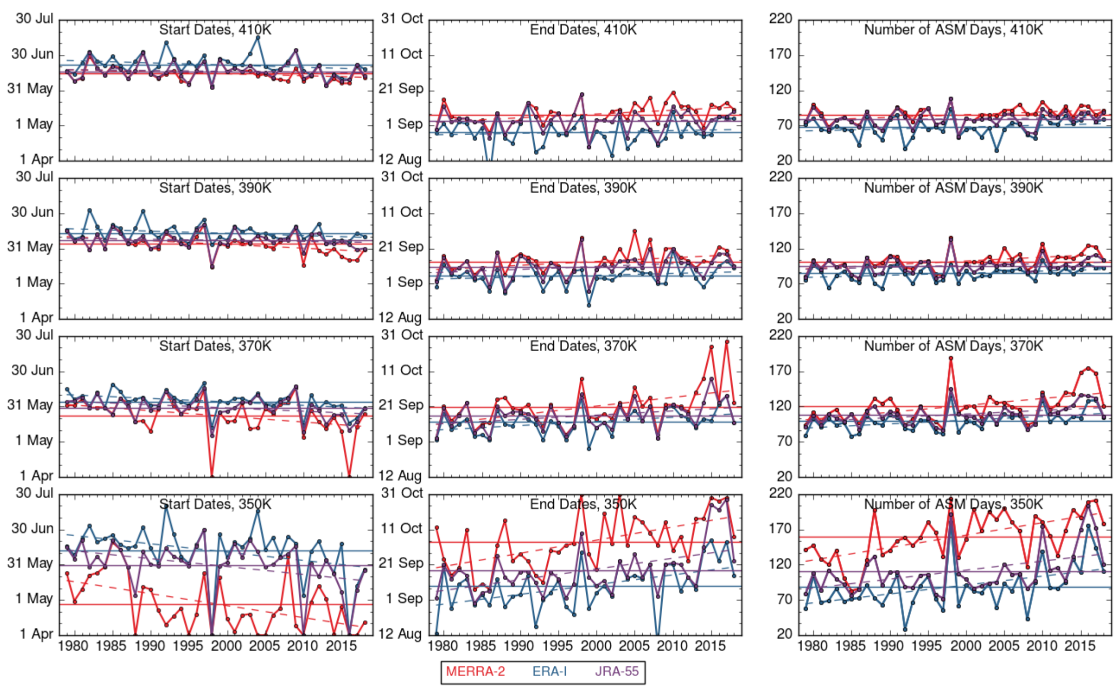

FIG. 6. Start dates, end dates, and duration of the monsoon season as defined in the text (Section 2b). Horizontal lines show each reanalysis' mean over the 40-year period. Overlaid dashed lines show linear fits to the values.

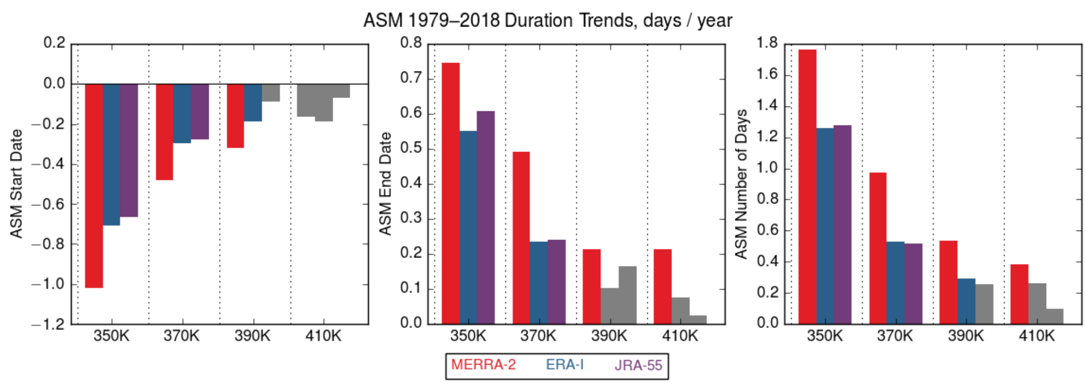

FIG. 7. Slopes of the linear fits to the start date, end date, and duration time series shown in Fig. 6. Bars in reanalysis colors indicate slopes that are significant at the 95% confidence level according to a permutation analysis (see Section 2b).

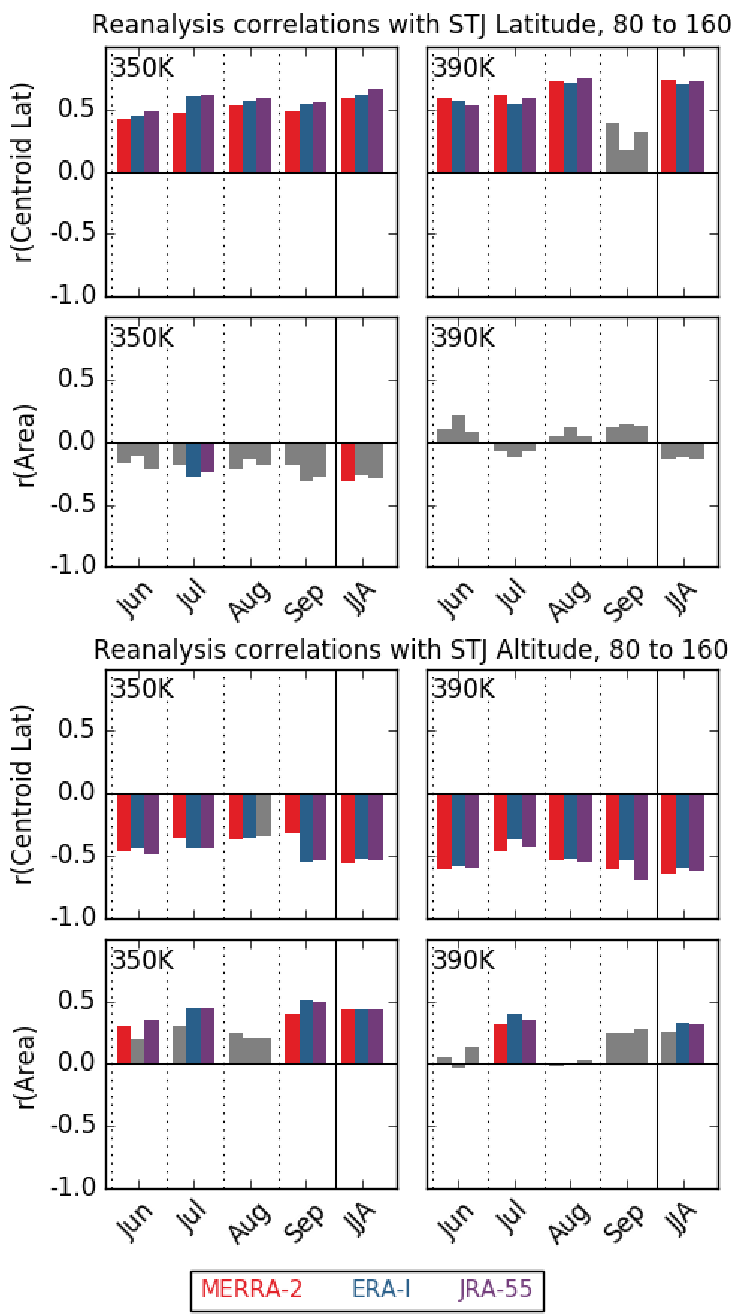

FIG. 8. Correlation between ASMA centroid latitude and area and subtropical upper tropospheric jet (see text for jet characterization method) latitude (top two rows) and altitude (bottom two rows) in the 80 to 160°E longitude band, at 350 K and 390 K. Correlations that are significant at the 95% level based on a bootstrapping analysis (Section 2b) are shown in the reanalysis colors.

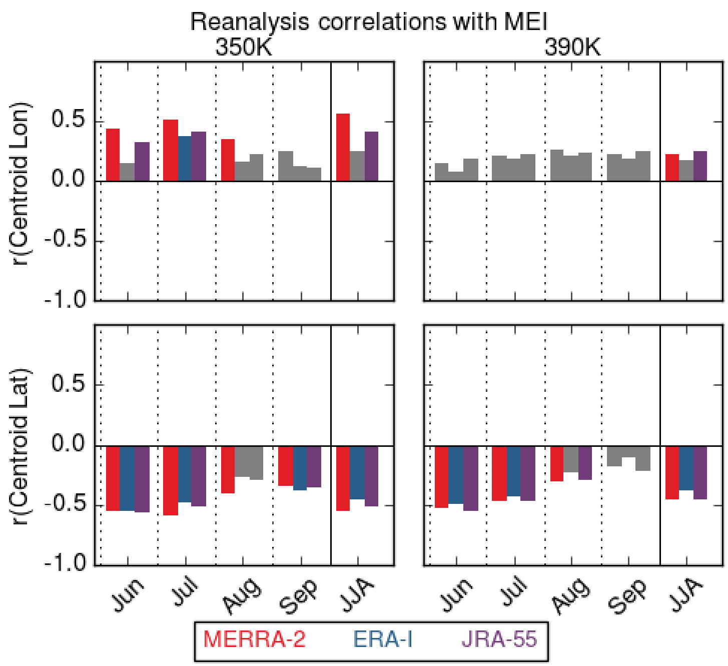

1162 FIG. 9. Correlations between ASMA centroid longitude and latitude and MEI index at 350 K and 390 K.
1163 Correlations that are significant at the 95% confidence level are shown in the reanalysis colors.

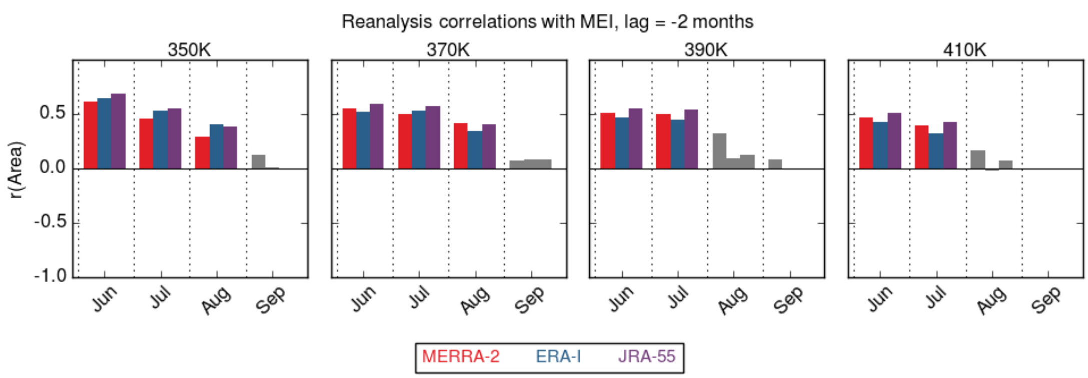

FIG. 10. Correlations between ASMA area and the MEI index with a 2-month lag. Correlations that are significant at the 95% confidence level are shown in the reanalysis colors.

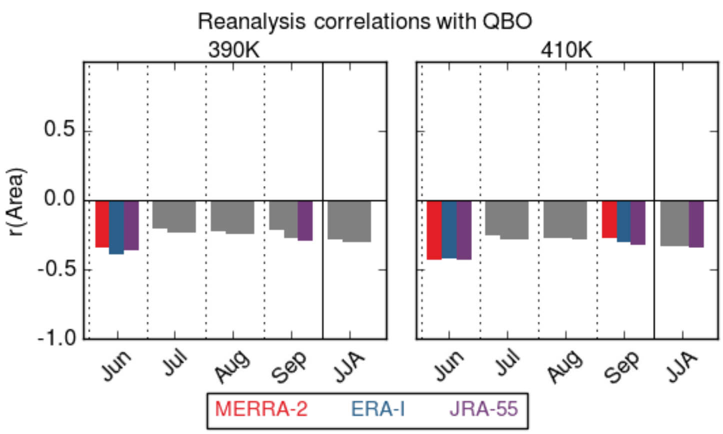

1166 FIG. 11. Correlations between ASMA area and the QBO index defined by Singapore winds at 70 hPa, at 390 K
1167 and 410 K. Correlations that are significant at the 95% confidence level are shown in the reanalysis colors.

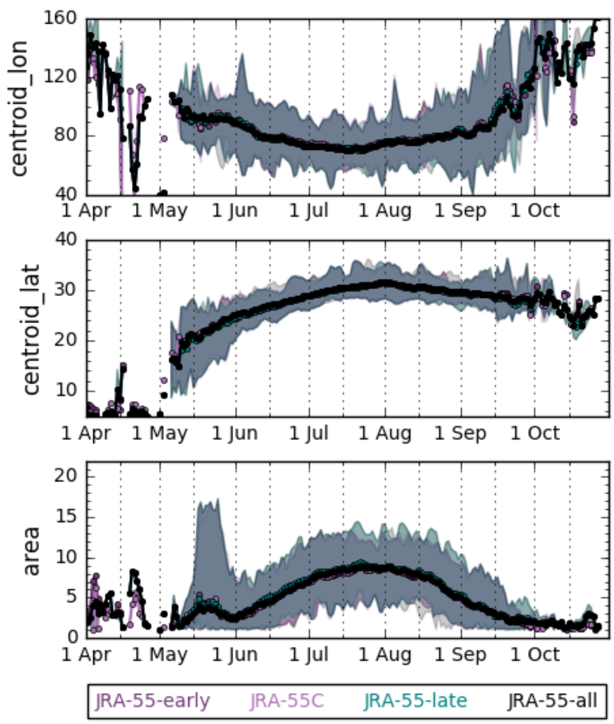

1168 FIG. 12. 370 K climatological (top to bottom) centroid longitude, centroid latitude, and area time series for JRA-55 & JRA-55C for 1973–2012 (purple & light purple, respectively), JRA-55 for 1979–2018 (teal), and JRA-55 for 1958–2018 (black).

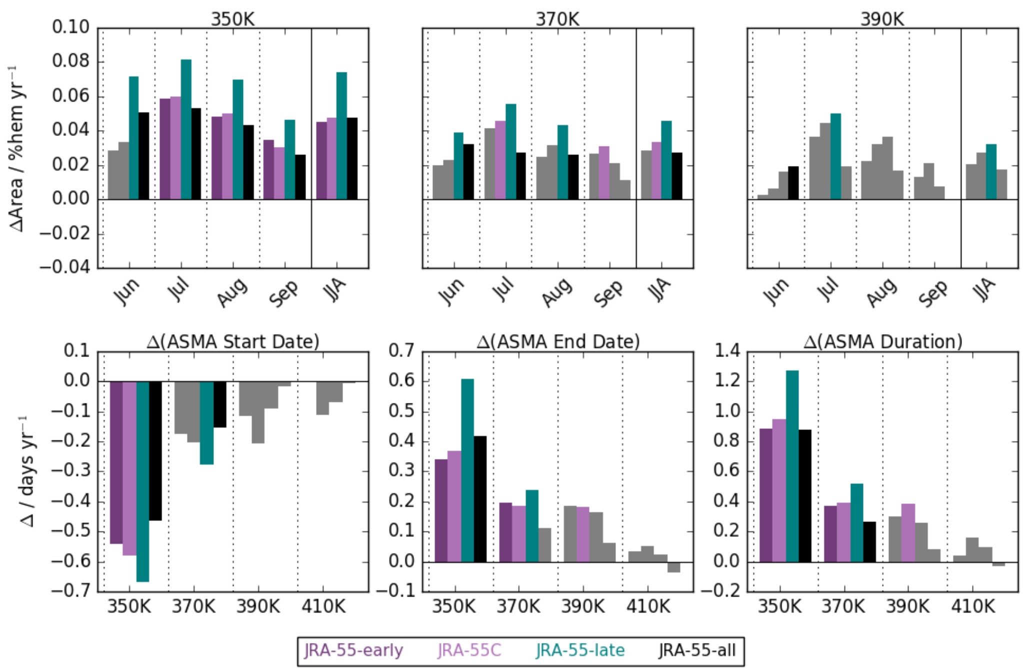

1171 FIG. 13. (Top) Slopes of linear fits to the area time series for the JRA-55(C) time series defined in Fig. 12 at
1172 350, 370, and 390 K. (Bottom) Slopes of fits to JRA-55(C) start and end dates and duration for the same periods.
1173 Bars in the reanalysis colors indicate slopes that are significant at the 95% confidence level.